Featured in Physics

Multiscale Physics of Atomic Nuclei from First Principles

Z. H. Sun,[1] A. Ekström,[2] C. Forssén,[2] G. Hagen,[1,3] G. R. Jansen,[4,1] and T. Papenbrock[3,1]

[1]*Physics Division, Oak Ridge National Laboratory, Oak Ridge, Tennessee 37831, USA*
[2]*Department of Physics, Chalmers University of Technology, SE-412 96 Göteborg, Sweden*
[3]*Department of Physics and Astronomy, University of Tennessee, Knoxville, Tennessee 37996, USA*
[4]*National Center for Computational Sciences, Oak Ridge National Laboratory, Oak Ridge, Tennessee 37831, USA*

(Received 26 March 2024; revised 10 September 2024; accepted 13 December 2024; published 10 February 2025)

Atomic nuclei exhibit multiple energy scales ranging from hundreds of MeV in binding energies to fractions of an MeV for low-lying collective excitations. As the limits of nuclear binding are approached near the neutron and proton drip lines, traditional shell structure starts to melt with an onset of deformation and an emergence of coexisting shapes. It is a long-standing challenge to describe this multiscale physics starting from nuclear forces with roots in quantum chromodynamics. Here, we achieve this within a unified and nonperturbative quantum many-body framework that captures both short- and long-range correlations starting from modern nucleon-nucleon and three-nucleon forces from chiral effective field theory. The short-range (dynamic) correlations which account for the bulk of the binding energy are included within a symmetry-breaking framework, while long-range (static) correlations (and fine details about the collective structure) are included by employing symmetry projection techniques. Our calculations accurately reproduce—within theoretical error bars—available experimental data for low-lying collective states and the electromagnetic quadrupole transitions in $^{20-30}$Ne. In addition, we reveal coexisting spherical and deformed shapes in ^{30}Ne, which indicates the breakdown of the magic neutron number $N = 20$ as the key nucleus ^{28}O is approached, and we predict that the drip line nuclei ^{32,34}Ne are strongly deformed and collective. By developing reduced-order models for symmetry-projected states, we perform a global sensitivity analysis and find that the subleading singlet S-wave contact and a pion-nucleon coupling strongly impact nuclear deformation in chiral effective field theory. The techniques developed in this work clarify how microscopic nuclear forces generate the multiscale physics of nuclei spanning collective phenomena as well as short-range correlations and allow one to capture emergent and dynamical phenomena in finite fermion systems such as atom clusters, molecules, and atomic nuclei.

DOI: 10.1103/PhysRevX.15.011028

Subject Areas: Computational Physics, Nuclear Physics, Quantum Physics

I. INTRODUCTION

Atomic nuclei exhibit emergent symmetry breaking: Deformation allows rotation and is identified by strong electromagnetic transitions, i.e., large $B(E2)$ values, within states that belong to a rotational band [1]. While this has been established knowledge for more than 70 years, the multiscale description of such phenomena with internucleon forces rooted in quantum chromodynamics has posed a long-standing challenge [2–16]. The situation is illustrated in Fig. 1. Binding energies, i.e., the negative of ground-state energies, are extensive quantities with about 8 MeV of binding per nucleon for medium-mass nuclei. The short range of the strong nuclear force implies that the bulk of the binding energy comes from short-range correlations in the wave function [17]. Furthermore, as nucleons are fermions that interact via two- and three-nucleon forces, these short-range correlations are dominated by two-particle–two-hole and three-particle–three-hole excitations. Such dynamical correlations can be captured efficiently by various methods, and the numerical cost grows polynomially with increasing mass number [18–22]. The recent *ab initio* [23] computation of the heavy nucleus ^{208}Pb [24], for instance, is impressive because of the computational size of the problem. However, this doubly magic nucleus has closed proton and neutron shells and, therefore, exhibits a simple spherical structure. One needs "only" to capture dynamical correlations when computing its ground state. In contrast, open-shell nuclei are deformed and exhibit rotations. These introduce the lowest energy scale in atomic nuclei and range from hundreds of keV in medium-mass nuclei to tens of keV in heavy ones [1];

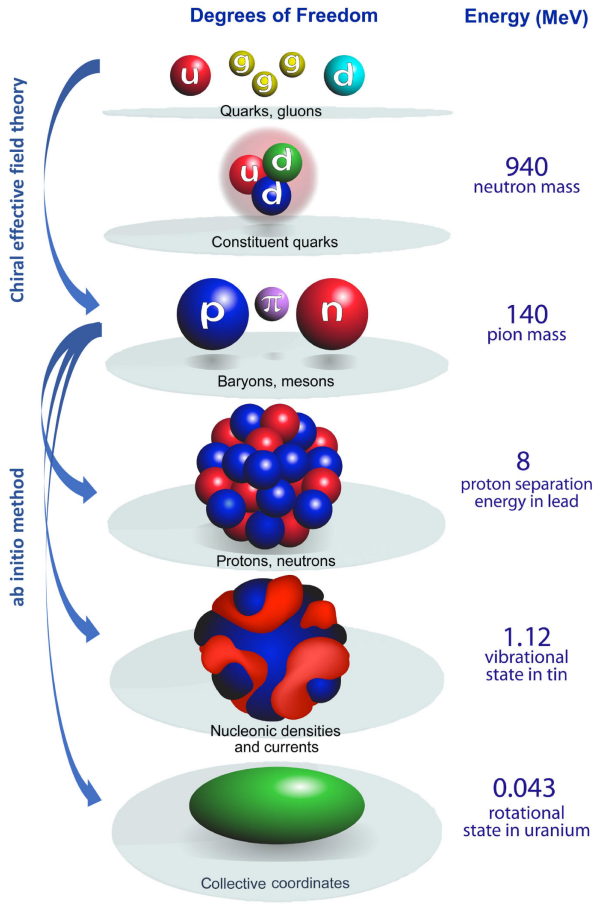

FIG. 1. Energy scales and relevant degrees of freedom in nuclear physics, adapted from Ref. [27] with permission from Witek Nazarewicz; see also Ref. [28]. Also shown are the tools employed in this work: We use chiral effective field theory to relate interactions between nucleons to quantum chromodynamics and coupled-cluster theory as an *ab initio* method for the computation of binding energies and collective excitations at the highest resolution scale [23].

see also Fig. 1. In the nucleus ^{34}Mg, for instance, the lowest rotational excitation is only 0.26% of the total binding energy [25]. This is a minuscule effect on the scale of nuclear energies that has a significant impact on the physics and shape of nuclei [26]. These collective modes involve long-range correlations that consist of many-particle–many-hole excitations. Such static correlations are difficult to capture.

It is no surprise then that the computation of deformed nuclei is more challenging and so far limited to light- and medium-mass nuclei [2–5,8–10,12,13,15]. The recent computations of deformed p-shell nuclei [4,5,12] and neon nuclei [9] underscore the importance of emergent symmetry breaking. However, these studies do not account for three-nucleon forces and—for neon—account for only a fraction of the binding energy. The calculations by Miyagi *et al.* [10] include three-nucleon forces but did not reproduce the strong electric quadrupole transitions within a rotational band. The calculations by Yao *et al.* [8] for ^{48}Ti reproduce $B(E2)$ values but at the expense of somewhat too stretched energy spectra. The computations by Frosini *et al.* [13] focus first on the static correlations and include dynamic correlations in a second step via perturbation theory. The latter accurately captures the binding energy only for sufficiently soft Hamiltonians (produced via a renormalization group transformation [29]), but that transformation changes the moment of inertia and thereby the collective properties; see Fig. 15 in Ref. [14].

In this work, we overcome these problems and demonstrate how to accurately capture multiscale physics of atomic nuclei starting from nuclear interactions rooted in quantum chromodynamics. We use the coupled-cluster [20,30] method for the nonperturbative inclusion of dynamical correlations and symmetry-projection techniques to capture static correlations. As we see, this approach also correctly reproduces the electromagnetic transitions in a rotational band. We employ the accurate chiral interaction 1.8/2.0(EM) of Ref. [31], which includes nucleon-nucleon forces at next-to-next-to-next-to-leading order (N3LO) and three-nucleon forces at next-to-next-to-leading order (NNLO). To better quantify our uncertainties in the predictions, we also employ an ensemble of posterior interaction samples from chiral effective field theory with explicit delta degrees of freedom at NNLO. This ensemble was obtained in a recent study of ^{28}O [32]. These interactions are described in detail in Sec. II A. In order to capture deformation, we start from an axially deformed Hartree-Fock reference state and include short-range correlations using the coupled-cluster method [20,30,33]. In a final step, we include long-range correlations by projecting the symmetry-broken coupled-cluster states on good angular momentum. Our projection is inspired by the disentangled approach by Qiu *et al.* [34] but avoids its shortcomings (i.e., asymmetric kernels) and extends it to electromagnetic transition matrix elements.

This work addresses the question—"what drives nuclear deformation?"—which has captivated generations of nuclear physicists [35–41]. Let us briefly summarize some milestones in the description of nuclear deformation: In the 1950s, Bohr [42], Bohr and Mottelson [43], and Nilsson [44] explained deformations as the surface vibrations of a liquid drop and the motion of independent nucleons confined inside [1]. In an alternative approach, Elliott and Cockcroft [45,46] explained how deformed intrinsic states can be understood within the spherical shell model. Dufour and Zuker [39] revisited deformation in the nuclear shell model and found it useful to decompose the Hamiltonian into monopole and multipole parts [47,48]. Here, the monopole essentially is the one-body normal-ordered term of the shell-model interaction, while the multipole terms are two-body operators; they contain the residual pairing and quadrupole interactions. These results have been succinctly summarized by Zuker's "multipole

proposes, monopole disposes" [40]; i.e., the competition between pairing and quadrupole-quadrupole interactions might suggest deformation, while the monopole—the effective spherical mean field—acts as a referee. We also note that the shell model uses phenomenological "effective charges" to reproduce electric quadrupole transitions [49]. Nuclear density functional approaches confirmed the important role of the proton-neutron quadrupole-quadrupole interactions [50,51]; these approaches accurately describe deformation across the nuclear chart [52–55].

While we have a good understanding of nuclear deformation at low resolution scales, we lack insights how the high-resolution interactions from effective field theories of quantum chromodynamics cause it to emerge. While the pairing interaction can readily be identified with the nucleon-nucleon interaction in the $^1S_0$ partial wave, the origin of the quadrupole-quadrupole interaction is opaque at best or a pure shell-model concept at worst. With a view on Ref. [37], one might be tempted to identify the quadrupole interaction with the isoscalar $^3D_2$ partial wave (which is attractive). However, the quadrupole-quadrupole interaction is long range—in contrast to the short-range nucleon-nucleon interaction—and it is applicable only in model spaces consisting of one-to-two shells [35]. Thus, our understanding of nuclear deformation is still limited to a low-resolution shell-model picture. The *ab initio* computations [4,9,13,15,56,57] reproduced deformed nuclei but did not investigate how they are shaped by the underlying forces. In this work, we seek to understand what impacts deformation at the highest resolution scale possible today, i.e., based on chiral effective field theory [58–60]. To that aim, we conduct a global sensitivity analysis [61] of collective nuclear properties and quantify how much individual terms in the chiral effective field theory interaction impact nuclear deformation. This global analysis is made possible using eigenvector continuation [62]. Specifically, we develop a reduced-order model [63] for emulating [64,65] *ab initio* calculations of deformed nuclei across millions of values for the low-energy constants in the chiral interaction. Our results are currently as close as we can get in tying low-energy nuclear structure to quantum chromodynamics without actually solving that non-Abelian gauge theory at low energies.

Finally, we address a challenging problem regarding the theoretical description of shape coexistence in nuclei [66–70]. The neutron-rich isotopes of neon and magnesium exhibit deformation and are a focus of experiments at rare isotope beam facilities [71–78]. In magnesium ($Z = 12$), shape coexistence has been observed in ^{30}Mg [72] and ^{32}Mg [74,79], and the drip line is thought to be beyond $N = 28$ [41,71,77,80]. The theoretical description of shape coexistence in ^{32}Mg has been a challenge [81–84]. The neon nuclei (proton number $Z = 10$) are less known. No shape coexistence has been observed in ^{30}Ne. The drip line nucleus is ^{34}Ne [76], and signatures of rigid rotation are found for ^{32}Ne [73,85]. The structure of ^{34}Ne and the quadrupole transition strengths of ^{32,34}Ne are unknown. This is a gap in our understanding in a critical region of the nuclear chart that extends toward the key nucleus ^{28}O [32]. For these reasons, we focus on neutron-rich isotopes of neon for discovery and use neutron-rich magnesium nuclei for validation.

This paper presents ideas, technical implementations, and predictions for quantities that are targeted in experiments. The main ideas consist of (i) capturing short-range (dynamic) correlations via a powerful many-body method and long-range (static) correlations via symmetry projection; (ii) to investigate how nuclear deformation is tied to the underlying forces from chiral effective field theory. The progress in technical implementation is in the symmetry projection itself and in the construction of a Hartree-Fock reduced-order model via eigenvector continuation. Finally, the predictions are about rotational energy levels and $B(E2)$ strengths in neutron-rich neon isotopes and shape coexistence in the $N = 20$ nucleus ^{30}Ne.

This paper is organized as follows. In Sec. II, we describe the theoretical framework. We introduce the Hamiltonian in Sec. II A, describe the computation of reference states in Sec. II B, and for completeness briefly review the coupled-cluster method in Sec. II C. Section II D presents a novel approach to angular-momentum projection within coupled-cluster theory applied to nuclei. In particular, this approach guarantees that norm and Hamiltonian kernels exhibit the correct symmetries. These developments might also be of interest for researchers in quantum chemistry. The computation of electromagnetic transition strengths is described in Sec. II E. In Sec. II F, we develop a reduced-order model for Hartree-Fock computations. This is a nontrivial extension of emulators based on eigenvector continuation, because one has to ensure that only Slater determinants (and not superpositions thereof) enter. We present results about the collective properties of neon isotopes (and predictions for ^{32,24}Ne) in Sec. III A. Predictions about the coexistence of a spherical and deformed shape in ^{30}Ne are presented in Sec. III B. Results from our global sensitivity analysis regarding nuclear deformation are presented in Sec. III C. Finally, we wrap up with a summary and discussion in Sec. IV. A number of details and supporting material are presented in the appendixes.

II. THEORETICAL FRAMEWORK

A. Hamiltonian and model space

We use the intrinsic Hamiltonian

$$H = T_{\text{kin}} - T_{\text{c.m.}} + V_{NN} + V_{NNN}. \tag{1}$$

Here, V_{NN} is the nucleon-nucleon (NN) potential, V_{NNN} the three-nucleon (NNN) potential, T_{kin} the total kinetic energy, and $T_{\text{c.m.}}$ the kinetic energy of the center of mass.

Using the intrinsic Hamiltonian effectively removes spurious center-of-mass motion [86].

We employ various interactions in this work. For point predictions, we use the 1.8/2.0(EM) [31] interaction that yields accurate binding energies and spectra of light-, medium-, and heavy-mass nuclei [87–92]. It consists of an *NN* potential at N3LO from Ref. [93], softened via similarity renormalization group transformation [29] to a momentum cutoff of 1.8 fm^{-1}, and a bare *NNN* potential at NNLO with a nonlocal regulator and a momentum cutoff of 2.0 fm^{-1}.

For posterior predictive distributions, incorporating relevant sources of uncertainty, we employ an ensemble of $n = 100$ interactions that was calibrated in light-mass nuclei and recently used for accurate predictions of nuclei around ^{28}O [32]. These interactions are from chiral effective field theory at NNLO with explicit delta degrees of freedom. The *NN* and *NNN* potentials have nonlocal regulators and a momentum cutoff of 394 MeV/c [94,95]. This ensemble was obtained in Ref. [32] and consists of prior interaction samples filtered out by history matching [24,96,97] to reproduce (within a nonimplausibility window) scattering phase shifts, deuteron properties, the binding energies and charge radii of ^{3}H, ^{4}He, and ^{16}O, and ground and excited states in ^{22,24,25}O. In order to use this ensemble for posterior predictions, we proceed as follows: We first assign likelihood weights $w_i = p(\mathcal{D}_{\mathrm{cal}}|\boldsymbol{\alpha}_i)$, with the excitation energies of the $J^\pi = 2^+$ and 4^+ rotational states in ^{24}Ne as calibration data $\mathcal{D}_{\mathrm{cal}}$ and $\boldsymbol{\alpha}_i$ a vector of low-energy constants from the ensemble. For this, we use a simple normal likelihood that incorporates uncertainties from method, model space, and effective field theory truncations (see Appendix C for details). We then employ importance resampling [98,99] with importance weights $q_i = w_i / \sum_{j=1}^{n} w_j$. This allows us to effectively collect samples from the posterior

$$p(\boldsymbol{\alpha}_i|\mathcal{D}_{\mathrm{cal}}) \propto p(\mathcal{D}_{\mathrm{cal}}|\boldsymbol{\alpha}_i)p(\boldsymbol{\alpha}_i). \tag{2}$$

Here, we use a prior, $p(\boldsymbol{\alpha}_i)$, that is uniform for all low-energy constants except for $c_{1,2,3,4}$, where it corresponds to a Gaussian distribution from a Roy-Steiner analysis of pion-nucleon scattering [100]. The posterior samples can then be used to make posterior predictions for rotational states and electromagnetic transitions in other nuclei (see Sec. III A). There is a rather large fraction of 59 samples that have importance weight within one order of magnitude from the largest one, $q_{\max}$, and the effective number of samples is $n_{\mathrm{eff}} \equiv \sum_{i=1}^{n} q_i / q_{\max} = 25$.

B. Normal-ordered two-body approximation and computation of the reference state

The inclusion of full *NNN* forces in coupled-cluster computations is possible [101] but expensive. Fortunately, it is not necessary for accurate computations: Once a reference state is determined, one can employ the normal-ordered two-body approximation and discard residual three-nucleon terms from the Hamiltonian [101–103].

For open-shell nuclei, however, the normal-ordered two-body Hamiltonian based on a deformed reference state breaks rotational symmetry. To avoid this problem, we follow Frosini *et al.* [104] and first perform a spherical Hartree-Fock computation based on a uniform occupation of the partially filled shells. The resulting spherical density matrix is then used to make the normal-ordered two-body approximation. The resulting normal-ordered two-body Hamiltonian is finally transformed back to the harmonic oscillator basis. This spherical two-body Hamiltonian is the starting point for our axially symmetric Hartree-Fock computation, which then yields the deformed reference state $|\Phi_0\rangle$.

Our Hartree-Fock computations use a spherical harmonic oscillator basis of up to 13 major shells, while the *NNN* interaction is further restricted by an energy cut $E_{3\,\max} = 16\hbar\omega$. To gauge the convergence of our results, we vary the harmonic oscillator frequency ($\hbar\omega$) from 10 to 16 MeV. Because of their computational cost, our angular-momentum-projected coupled-cluster calculations are restricted to 8–9 major shells. This is sufficient to obtain spectra and quadrupole transitions that are converged with respect to the size of the model space for the nuclei we compute (see Appendix B for details).

The computation of deformed reference states gives us the flexibility to study shape coexistence by targeting different deformations. The simplest approach is to fill the open shells according to the Nilsson model [44] when initializing the density matrix for the ensuing Hartree-Fock computation. This allows one to construct prolate or oblate references. When computing nuclei with the "magic" neutron number $N = 20$, this usually leads to reference states with a small deformation. Strongly deformed references can be obtained by adding the quadrupole constraint $\lambda r^2 Y_{20}(\hat{\mathbf{r}})$ to the Hamiltonian and by varying the Lagrange multiplier λ such that a local energy minimum results (as a function of the quadrupole expectation value) [105]. Thus, this is an important tool to study shape coexistence along the $N = 20$ line for neutron-rich nuclei.

C. Coupled-cluster calculations include dynamical correlations

Our coupled-cluster computations [20,30,33,106] start from an axially symmetric Hartree-Fock reference state $|\Phi_0\rangle$ with prolate deformation [15,107]. For a nucleus with mass number A, the coupled-cluster method parametrizes the many-nucleon wave function as $|\Psi\rangle = e^T|\Phi_0\rangle$, with $T = T_1 + T_2 + \cdots + T_A$ being an expansion in n-particle–n-hole (np–nh) excitations ($n = 1, \ldots, A$). To compute observables and transitions consistently, we use the bivariational coupled-cluster energy

functional [108,109], where the left coupled-cluster state is parametrized as $\langle\tilde{\Psi}| = \langle\Phi_0|(1+\Lambda)e^{-T}$ with Λ containing up to np–nh deexcitations and truncated at the same order as T. For systems with a well-defined Fermi surface, the dynamical correlations—accounting for the bulk of the binding energy—are effectively captured by truncating $T \approx T_1 + T_2$, known as the coupled-cluster singles-and-doubles approximation (CCSD), and including T_3 perturbatively [20,33]. This results in a polynomial scaling of computational cost of the order of N^6 (or at most N^7), where N is a measure of the system size [33]. In both quantum chemistry and nuclear physics applications, CCSD is found to capture about 90% of the full correlation energy. The inclusion of triples corrections brings that number up to about 99% [20,33,110]. In Appendix B, we show that this is also the case for the deformed $^{20-34}$Ne isotopes using the 1.8/2.0(EM) chiral interaction.

D. Angular-momentum projection captures static correlations

We perform angular-momentum projections of deformed states computed in the CCSD approximation. For a more accurate angular-momentum projection than in Ref. [15], we use the bivariational coupled-cluster energy functional [108,109]

$$E^{(J)} = \frac{\langle\tilde{\Psi}|P_J H|\Psi\rangle}{\langle\tilde{\Psi}|P_J|\Psi\rangle}. \tag{3}$$

Here, $|\Psi\rangle \equiv e^T|\Phi_0\rangle$ is the right coupled-cluster state and $\langle\tilde{\Psi}| \equiv \langle\Phi_0|(1+\Lambda)e^{-T}$ is the corresponding left ground state. P_J is the angular-momentum projection operator

$$P_J = \frac{2J+1}{2}\int_0^\pi d\beta d^J_{00}(\beta)R(\beta), \tag{4}$$

and $R(\beta) = e^{-i\beta J_y}$ is the rotation operator. P_J projects an axially symmetric state with $J_z = 0$ onto a state with angular momentum J. This operator employs the "small" Wigner $d^J_{00}(\beta)$ function, and J_y is the y component of the total angular momentum. To evaluate Eq. (3), we use the CCSD approximation and build on the disentangled approach by Qiu *et al.* [34]. This approach applies the Thouless theorem [111] to act with the rotation operator $R(\beta)$ on the symmetry-broken reference state, i.e., $\langle\Phi_0|R(\beta) = \langle\Phi_0|R(\beta)|\Phi_0\rangle\langle\Phi_0|e^{V(\beta)}$, with $V(\beta)$ being a $1p$–$1h$ deexcitation operator. Next, one expands

$$e^{V(\beta)}e^T = e^{W_0(\beta)+W_1(\beta)+W_2(\beta)+\cdots}. \tag{5}$$

The series of np–nh excitation operators W_n does not truncate (even for $T \approx T_1 + T_2$) and includes up to Ap–Ah excitations.

In this work, we keep only the amplitudes W_0, W_1, and W_2. Qiu *et al.* [34] proposed to compute the amplitudes W_0, W_1, and W_2 by taking the derivative of Eq. (5) with respect to β. This leads to a set of ordinary differential equations with the initial ($\beta = 0$) values $W_0(0) = 0$, $W_1(0) = T_1$, and $W_2(0) = T_2$. This approach has two disadvantages: First, $dV(\beta)/d\beta$ can have very large matrix elements in cases where the rotated state has a small overlap with the reference state, i.e., for $\langle\Phi_0|R(\beta)|\Phi_0\rangle \approx 0$. This leads to a "stiffness" in the set of ordinary differential equations. Second, as one integrates the differential equations starting at $\beta = 0$, the truncation at W_2 may lead to a loss of accuracy for larger angles. This loss of accuracy manifests itself, for instance, in a lack of symmetry of norm and Hamiltonian kernels under $\beta \to \pi - \beta$ for even-even nuclei; see Fig. 2 for a numerical demonstration for the case of ^{20}Ne.

To avoid these problems, we propose a new method (see also Ref. [113]) to solve Eq. (5), where we instead consider the expression

$$e^{\lambda V}e^T = e^{W_0(\lambda)+W_1(\lambda)+W_2(\lambda)+\cdots}, \tag{6}$$

which, for $\lambda = 1$, agrees with the previous one. Taking the derivative of Eq. (6) with respect to λ at fixed angle β yields a new set of ordinary differential equations. We integrate over λ from 0 to 1, and the initial values are

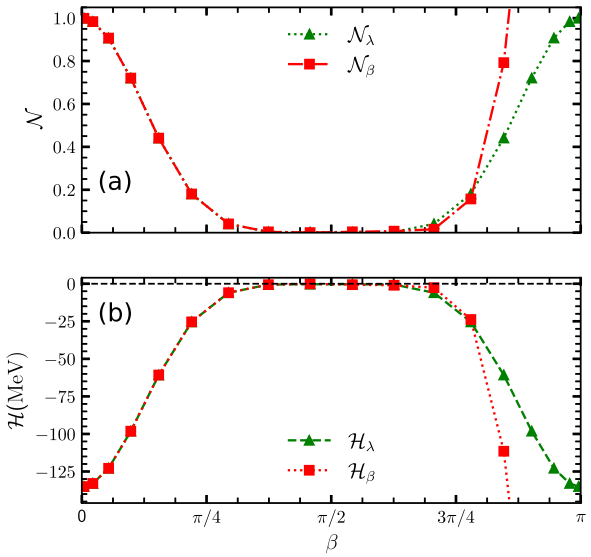

FIG. 2. (a) shows the norm kernels for ^{20}Ne computed in the traditional disentangled approach (red, dash-dotted line) and with the new method of this work (green, dashed line). (b) shows the same as (a) but for the Hamiltonian kernel. All calculations used the NNLO$_{\text{opt}}$ interaction [112] with $\hbar\omega = 14$ MeV in a model space of $N_{\max} = 8$. The kernels ($\mathcal{H}_\beta$ and $\mathcal{N}_\beta$) are the solutions of the differential equation when taking the derivative of Eq. (5) with respect to β, while ($\mathcal{H}_\lambda$ and $\mathcal{N}_\lambda$) are the solutions of the differential equation when taking the derivative of Eq. (6) with respect to λ.

$W_n(\lambda = 0) = T_n$. These equations are solved at fixed β. Note that we suppress the dependence of V and W_n on β in Eq. (6). This approach significantly improves the stability of the numerical integration, keeps kernels symmetric under $\beta \to \pi - \beta$, and yields more accurate results for larger angles β. Results are shown in Fig. 2. Nevertheless, the truncation at W_2 implies that the projection operator P_J is not treated exactly, and angular momentum is only approximately a good quantum number.

E. Electromagnetic transition strengths

The accurate computation of electromagnetic transitions strength in nuclei using *ab initio* methods has been a long-standing challenge [10,114–116]. In this work, we overcome this challenge by using symmetry projection techniques to capture the fine details in the nuclear wave function that drives quadrupole collectivity.

The electric quadrupole ($E2$) transition strength

$$B(E2,\downarrow) \equiv |\langle 0^+||Q_2||2^+\rangle|^2 \tag{7}$$

is determined by the reduced matrix element $\langle 0^+\|Q_2\|2^+\rangle = \langle 0^+, J_z = 0\|Q_{20}\|2^+, J_z = 0\rangle / C^{00}_{2020}$. Here, $Q_{20} = \sum_j e(1/2 - \tau_z^{(j)})\, r_j^2 Y_{20}(\hat{\mathbf{r}}_j)$ is the electric quadrupole operator (given in terms of the electric charge e, the isospin operators $\tau_z^{(j)}$, and positions $\mathbf{r}_j$ of the nucleon labeled by j, and the spherical harmonics Y_{20}), and C^{00}_{2020} is a Clebsch-Gordan coefficient.

As coupled-cluster theory is based on a bivariational functional, we need to compute

$$\begin{aligned} B(E2,\downarrow) &= \frac{\langle\tilde{\Psi}|P_0 Q_{20} P_2|\Psi\rangle\langle\tilde{\Psi}|P_2 Q_{20} P_0|\Psi\rangle}{\langle\tilde{\Psi}|P_0|\Psi\rangle\langle\tilde{\Psi}|P_2|\Psi\rangle} \\ &= \frac{\langle\tilde{\Psi}|P_0 Q_{20}|\Psi\rangle\langle\tilde{\Psi}|Q_{20} P_0|\Psi\rangle}{\langle\tilde{\Psi}|P_0|\Psi\rangle\langle\tilde{\Psi}|P_2|\Psi\rangle}, \end{aligned} \tag{8}$$

where we remove redundant P_2 operators in the last step [117]. We recall that $|\Psi\rangle \equiv e^T|\Phi_0\rangle$ is the right coupled-cluster state and $\langle\tilde{\Psi}| \equiv \langle\Phi_0|(1+\Lambda)e^{-T}$ is the corresponding left ground state. Let us consider the computation of the matrix elements entering the numerator of Eq. (8). The projector is based on the rotation operator R (here, we suppress the dependence on β), and we have

$$\langle\tilde{\Psi}|RQ_{20}|\Psi\rangle = \langle\Phi_0|R|\Phi_0\rangle\langle\Phi_0|\tilde{Z}\bar{Q}_{20}e^{W_0+W_1+W_2}|\Phi_0\rangle, \tag{9}$$

with

$$\tilde{Z} = e^V R^{-1}(1+\Lambda)e^{-T}Re^{-V}, \tag{10}$$

$$\bar{Q}_{20} = e^V Q_{20} e^{-V}. \tag{11}$$

Note that $\tilde{Z}$ contains up to $2p$–$2h$ deexcitations and that $\bar{Q}_{20}$ is a one-body similarity transformed operator. The second part of the transition matrix element is

$$\begin{aligned} \langle\tilde{\Psi}|Q_{20}R|\Psi\rangle &= \langle\tilde{\Psi}|RR^{-1}Q_{20}R|\Psi\rangle \\ &= \langle\Phi_0|R|\Phi_0\rangle\langle\Phi_0|\tilde{Z}\tilde{Q}_{20}e^{W_0+W_1+W_2}|\Phi_0\rangle, \end{aligned} \tag{12}$$

with

$$\tilde{Q}_{20} = e^V R^{-1} Q_{20} R e^{-V}. \tag{13}$$

In Appendix B, we benchmark our approach with the symmetry-adapted no-core shell model [11] in ^{20}Ne using the nucleon-nucleon potential NNLO$_{\text{opt}}$ [112] and find agreement within estimated uncertainties.

F. A reduced-order model for projection-after-variation Hartree-Fock

We utilize eigenvector continuation [62] to construct a reduced-order model [63] of Hartree-Fock. This enables us to develop fast and accurate emulators [64,65] necessary for performing the sensitivity analyses presented in Sec. III C. We begin by exploiting that the delta-full NNLO Hamiltonian with NN and NNN interactions is a sum of terms with a linear dependence on the 17 low-energy constants ($\boldsymbol{\alpha}$) of interest, i.e.,

$$H(\boldsymbol{\alpha}) = H_0 + \sum_{i=1}^{17} \alpha_i H_i. \tag{14}$$

Here, H_i denote the respective Hamiltonian terms, and $H_0 = T_{\text{kin}} + V_0$ is the intrinsic kinetic energy T_{kin} and V_0 denotes $\boldsymbol{\alpha}$-independent potential contributions such as one-pion exchange, leading two-pion exchange, and the Fujita-Miyazawa [118] NNN interaction.

Let us consider a Hartree-Fock state $|\phi_i\rangle \equiv |\phi(\boldsymbol{\alpha}_i)\rangle$, with corresponding energy $E_{\text{HF}}(\boldsymbol{\alpha}_i)$ for some vector of values $\boldsymbol{\alpha}_i$. Clearly, the corresponding Hartree-Fock Hamiltonian is a one-body operator $H_{\text{HF}}(\boldsymbol{\alpha}_i)$ that fulfills

$$H_{\text{HF}}(\boldsymbol{\alpha}_i)|\phi_i\rangle = E_{\text{HF}}(\boldsymbol{\alpha}_i)|\phi_i\rangle. \tag{15}$$

In general, given any Slater determinant $|\phi\rangle$, we can normal-order the Hamiltonian (14) with respect to $|\phi\rangle$ and obtain

$$H(\boldsymbol{\alpha}) = E_\phi(\boldsymbol{\alpha}) + F_\phi(\boldsymbol{\alpha}) + W_\phi(\boldsymbol{\alpha}), \tag{16}$$

where $E_\phi(\boldsymbol{\alpha}) = \langle\phi|H(\boldsymbol{\alpha})|\phi\rangle$, $F_\phi(\boldsymbol{\alpha})$ is the normal-ordered one-body Fock operator, and $W_\phi(\boldsymbol{\alpha})$ denotes any remaining terms. We have, in particular,

$$H_{\text{HF}}(\boldsymbol{\alpha}_i) = E_{\phi_i}(\boldsymbol{\alpha}_i) + F_{\phi_i}(\boldsymbol{\alpha}_i). \tag{17}$$

We now seek to emulate the exact Hartree-Fock energy $E_{\mathrm{HF}}(\boldsymbol{\alpha}_{\odot})$ for some target value $\boldsymbol{\alpha}=\boldsymbol{\alpha}_{\odot}$ of the low-energy constants. To that end, we use eigenvector continuation [62] and expand the target wave function in a small set of Hartree-Fock states $|\phi_i\rangle$, i.e., a so-called snapshot basis, such that

$$|\phi_{\odot}\rangle \approx \sum_{i=1}^{N_{\mathrm{train}}} c_i |\phi_i\rangle. \tag{18}$$

The snapshot basis spans a low-dimensional subspace into which the Hartree-Fock Hamiltonian can be projected, thereby achieving a model-order reduction. We use the decomposition in Eq. (14) to project the individual interaction terms of the Hartree-Fock Hamiltonian to the subspace independently of $\boldsymbol{\alpha}$. This enables fast and accurate emulation of the Hartree-Fock energy $E_{\mathrm{HF}}(\boldsymbol{\alpha}_{\odot})$ in the subspace for any target value $\boldsymbol{\alpha}_{\odot}$ by solving the generalized eigenvalue problem

$$\sum_{ij}\langle\phi_i|H_{\mathrm{HF}}(\boldsymbol{\alpha}_{\odot})|\phi_j\rangle c_j = E_{\odot}\sum_{ij}\langle\phi_i|\phi_j\rangle c_j. \tag{19}$$

In our applications (see Sec. III C), we find $E_{\odot}\approx E_{\mathrm{HF}}(\boldsymbol{\alpha}_{\odot})$ with very high accuracy and precision using a very small basis of $N_{\mathrm{train}}=68$ snapshots.

It is important to recognize that the exact states, i.e., the snapshots, must be product states. Thus, one must not replace H_{HF} in Eq. (19) with the full Hamiltonian, because this would correspond to the generator coordinate method (GCM) [119,120] with the low-energy constants $\boldsymbol{\alpha}$ as continuous parameters. In the GCM case, one would not reproduce the Hartree-Fock snapshots for $\boldsymbol{\alpha}_{\odot}=\boldsymbol{\alpha}_i$ but rather obtain states corresponding to a lower energy from superpositions of product states.

To construct the Hartree-Fock Hamiltonian $H_{\mathrm{HF}}(\boldsymbol{\alpha}_{\odot})$ in the subspace spanned by the snapshot basis, we proceed as follows. We write the Hartree-Fock solution $|\phi_i\rangle$ for the snapshot value $\boldsymbol{\alpha}_i$ as $|\phi_i\rangle=U_i|\Phi_0\rangle$, where $|\Phi_0\rangle$ is a reference state in the underlying harmonic-oscillator basis. The norm and Hamiltonian kernels for the generalized eigenvalue problem in the subspace (19) are

$$\langle\phi_i|\phi_j\rangle = \langle\Phi_0|\mathcal{O}_{ij}|\Phi_0\rangle, \tag{20}$$

$$\langle\phi_i|H_{\mathrm{HF}}(\boldsymbol{\alpha}_{\odot})|\phi_j\rangle = \langle\Phi_0|\mathcal{O}_{ij}h_j(\boldsymbol{\alpha}_{\odot})|\Phi_0\rangle. \tag{21}$$

Here, $\mathcal{O}_{ij}=U_i^{\dagger}U_j$ is a unitary matrix, and $h_j(\boldsymbol{\alpha}_{\odot})=U_j^{\dagger}H_{\mathrm{HF}}(\boldsymbol{\alpha}_{\odot})U_j$. With a view on Eq. (17), we now define

$$H_{\mathrm{HF}}(\boldsymbol{\alpha}_{\odot}) = E_{\phi_j}(\boldsymbol{\alpha}_{\odot}) + F_{\phi_j}(\boldsymbol{\alpha}_{\odot}); \tag{22}$$

i.e., the Hartree-Fock Hamiltonian at the target value consists of the zero-body and one-body terms of the target Hamiltonian normal ordered with respect to the Hartree-Fock state at snapshot value $\boldsymbol{\alpha}_j$.

We note that the Hamiltonian kernel in Eq. (21) is not symmetric, and the Fock matrix $F_{\phi_j}(\boldsymbol{\alpha}_{\odot})$ is not diagonal for $\boldsymbol{\alpha}_{\odot}\neq\boldsymbol{\alpha}_j$. This is an important point, and it ensures that—at a snapshot value—the solution of the generalized eigenvalue problem is indeed an eigenstate of the Hartree-Fock Hamiltonian (and not a GCM solution that is lower in energy). The norm kernel for nonorthogonal reference states is given by [121]

$$\langle\Phi_0|\mathcal{O}_{ij}|\Phi_0\rangle = \det(\mathcal{O}_{ij}^{hh}), \tag{23}$$

where $\mathcal{O}_{ij}^{hh}$ is the matrix of overlaps between occupied (hole) states in $\langle\phi_i|$ and $|\phi_j\rangle$. To evaluate the Hamiltonian kernel, we utilize the Thouless theorem [111] and write

$$\langle\Phi_0|\mathcal{O}_{ij} = \langle\Phi_0|\mathcal{O}_{ij}|\Phi_0\rangle\langle\Phi_0|e^{V}, \tag{24}$$

with V being a $1p$–$1h$ deexcitation operator. The matrix elements of V in the hole-particle (hp) space is given by the matrix product [34]

$$V^{hp} = (\mathcal{O}_{ij}^{hh})^{-1}\mathcal{O}_{ij}^{hp}. \tag{25}$$

Inserting Eq. (24) into Eq. (21), we obtain the algebraic equation

$$\langle\phi_i|H_{\mathrm{HF}}(\boldsymbol{\alpha}_{\odot})|\phi_j\rangle = \langle\phi_i|\phi_j\rangle\left(E_{\mathrm{HF}}+\sum_{hp}V_p^hF_h^p\right). \tag{26}$$

Here, E_{HF} and F are the vacuum energy and one-body normal ordered terms, respectively, of $H_{\mathrm{HF}}(\boldsymbol{\alpha}_{\odot})$ with respect to $|\phi_j\rangle$.

The norm and Hamiltonian Hartree-Fock kernels can also be evaluated using a generalized Wick's theorem [121–124]. We verified that this alternative approach gives results that agree with the one used in this work. Having obtained the reduced-order model for the target Hartree-Fock state by diagonalizing the generalized nonsymmetric eigenvalue problem in Eq. (19), we evaluate the projected target Hartree-Fock energies from

$$E_{\odot}^{(J)} = \frac{\langle\phi_{\odot}|P_JH(\boldsymbol{\alpha}_{\odot})|\phi_{\odot}\rangle}{\langle\phi_{\odot}|P_J|\phi_{\odot}\rangle}. \tag{27}$$

Here, the full target Hamiltonian in Eq. (14) enters, and P_J is the projection operator.

III. RESULTS

Ab initio computations of realistic ground-state energies for spherical light- and medium-mass nuclei are demanding calculations but can nowadays be performed routinely [125]. In this work, however, we focus on our

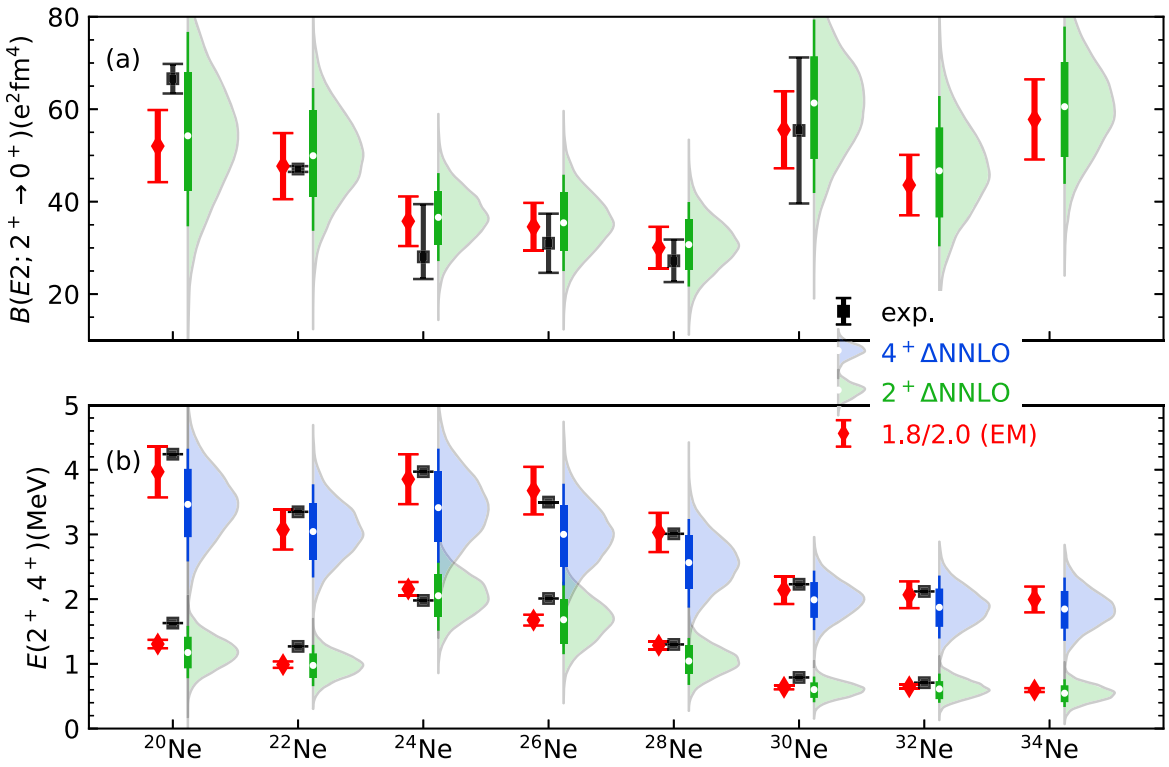

FIG. 3. (a) shows electric quadrupole transition strengths from the first excited 2^+ state to the ground state, while (b) shows energies of the lowest 2^+ and 4^+ states in the even nuclei $^{20-34}$Ne. Theoretical results are computed using angular-momentum-projected coupled-cluster. Point predictions using the interaction 1.8/2.0(EM) [31] (red diamonds with one standard deviation uncertainty estimates from many-body method and model-space truncations) are shown together with full posterior predictive distributions using the delta-full NNLO interaction ensemble (ΔNNLO), including sampling of method and model errors. For the latter, 68% and 90% credible intervals are shown as a thick and thin vertical bar, respectively, and the median is marked as a white circle. The posterior predictive distributions are obtained using importance resampling. Experimental data [126] (and Refs. [73,85] for ^{32}Ne) are shown as black squares with error bars.

novel results for deformation and shape coexistence emerging in a multiscale setting encompassing both small excitation energies and large total binding energies.

A. Multiscale physics of neutron-rich neon nuclei

Let us study first the collective properties of neon nuclei. The results for even-mass isotopes are shown in Fig. 3. The lower panel shows the excitation energies $E(2^+)$ and $E(4^+)$ of the lowest spin-parity $J^\pi = 2^+$ and 4^+ states, respectively, in the $^{20-32}$Ne compared with available experimental data. The results based on the 1.8/2.0(EM) interaction are marked by red diamonds and include uncertainty estimates from method and model-space truncations. The relative accuracy of our calculations with the interaction 1.8/2.0(EM) is about 2%–3%. The distributions labeled ΔNNLO are posterior predictive distributions and based on the results of $n = 100$ symmetry-projected coupled-cluster computations (one for each member of the interaction ensemble). They are given by the set

$$\{y_k(\boldsymbol{\alpha}) + \varepsilon_{\mathrm{MB}} + \varepsilon_{\mathrm{EFT}} \colon \boldsymbol{\alpha} \sim p(\boldsymbol{\alpha}|\mathcal{D}_{\mathrm{cal}})\}, \tag{28}$$

where y_k is the *ab initio* model prediction for observable k while $\varepsilon_{\mathrm{MB}}$ and $\varepsilon_{\mathrm{EFT}}$ are samples from the stochastic models for errors due to the many-body method and model-space truncation and the truncation of the effective field theory expansion, respectively (see Appendix C for details). When generating the posterior predictive distributions, we use 10000 samples from the posterior $p(\boldsymbol{\alpha}|\mathcal{D}_{\mathrm{cal}})$ obtained via importance resampling (see Sec. II A). We also show 68% and 90% credible intervals around the median value. These uncertainty estimates are consistent with data (given the small number of data points): Out of 14 measured energies, six and 13 are within the 68% and 90% credible interval, respectively. It might be, however, that the 68% interval is slightly underestimated. For the point prediction, one would interpret the (one-sigma) error bar as indicating the uncertainty in the results based on the model-space truncation and method error. We see that eight out of 14 energies are within the uncertainties, although only one of the 2^+ energies is within uncertainties.

Theoretical results are consistent with each other and accurately reproduce the experimental trend where data exist. For neon nuclei with neutron number below $N = 20$,

i.e., ^{30}Ne, the ΔNNLO posterior predictive distributions indicate somewhat too compressed spectra. For neutron number $N \geq 20$, the excitation energies follow the pattern $E(J) = J(J+1)/(2\Theta)$ of a rigid rotor, and the relatively small values reflect a large moment of inertia Θ and a strong deformation. The computed energy-ratio $R_{42} \equiv E(4^+)/E(2^+)$ values of ^{34}Ne are 3.37 ± 0.13 from the posterior (68% credible interval) and 3.38 ± 0.12 for 1.8/2.0(EM); both are close to the value 10/3 of a rigid rotor. Results for the drip line nucleus ^{34}Ne are predictions.

The upper panel in Fig. 3 shows the computed electric quadrupole transition strength from the first excited 2^+ state to the 0^+ ground state. Overall, theory agrees with data, though both theoretical and experimental uncertainties are substantial. Here, all six data points are already within the 68% credible interval for the ΔNNLO ensemble. For the point prediction, five out of six data points are within the one-sigma uncertainty. For ^{30}Ne, theory is as precise as data, and we make equally precise predictions for ^{32,34}Ne.

These results demonstrate that the inclusion of short- and long-range correlations on top of an axially deformed reference state enables one to accurately capture quadrupole collectivity. The resulting picture is simple and well aligned with ideas from effective field theories where short-range and long-range correlations are distinguished. The symmetry-breaking Hartree-Fock state provides us with a leading-order description of the nucleus and yields the Fermi momentum as a dividing scale. Short-range (high-momentum) contributions are included via few-particle–few-hole excitations within standard coupled-cluster theory; this yields almost all binding energy. Long-range correlations enter as a higher-order correction via many-particle–many-hole excitations and are included by symmetry projection of the correlated and symmetry-broken coupled-cluster state. This contributes little energy to the binding of the nucleus but is essential for its collective structure. This combined approach overcomes a long-standing multiscale challenge in low-energy nuclear physics [10,68,114,116,127].

We also compute rotational bands for magnesium isotopes. These nuclei are much better known than the neon isotopes. For this reason, we limit ourselves to the 1.8/2.0(EM) potential and perform only projected Hartree-Fock calculations. The result are close to data and shown for completeness in Appendix D.

B. Shape coexistence in ^{30}Ne and ^{32}Mg

The nuclei ^{30}Ne and ^{32}Mg are particularly interesting, as they contain 20 neutrons, which is a magic number in the traditional shell model [128]. Though these nuclei are deformed in their ground state [129,130], signatures of the $N = 20$ magic number can be seen in our calculations and lead to shape coexistence. While it would be most interesting to study shape coexistence with the ensemble of ΔNNLO interactions, the computational cost is beyond the scope of this work. Therefore, the following calculations are based on the 1.8/2.0(EM) interaction. This interaction is known to be most accurate for binding energies and spectra. For comparison, we briefly present results obtained for the standard parametrization of the $\Delta\text{NNLO}_{\text{GO}}(394)$ interaction [95].

For ^{30}Ne and ^{32}Mg, we perform constrained quadrupole-moment Hartree-Fock calculations, as described in Sec. II B, starting from a spherical harmonic oscillator basis with oscillator frequency $\hbar\omega = 14$ MeV. In both nuclei, we find one minimum corresponding to a more spherical shape plus a second one with strong deformation; see Figs. 4(a) and 5(a). The near-spherical configurations are close in energy to the well-deformed ones. This suggests that the shape coexistence, observed for $N = 20$ in ^{32}Mg [74], remains present when two protons are removed from that nucleus. We note that the more spherical and well-deformed Hartree-Fock states exhibit different occupations of Nilsson orbitals. The more spherical states reflect the $N = 20$ subshell closure for neutrons. For the deformed states, two intruder orbitals with $j_z = \pm 1/2$ from the pf shell are occupied. As we work in a single-reference framework (and do not break particle numbers as in Hartree-Fock Bogoliubov), there is no continuous connection between the two different Hartree-Fock energy "surfaces." One can relate the quadrupole expectation values q_{20} to the quadrupole deformation parameter β_2 via $\beta_2 = \sqrt{5\pi} q_{20}/(3AR_0^2)$, where $R_0 = 1.2A^{1/3}$ fm [131]. Using this relation, one gets $\beta_2 = 0.10$ and 0.44 for the near-spherical and deformed minimum in ^{30}Ne, respectively. For ^{32}Mg, the corresponding values are $\beta = 0.11$ and 0.43.

Figures 4(b), 4(c), 5(b), and 5(c) demonstrate the vast difference of scales of the computed binding energies E and the rotational excitation energies E^*. Both scales simultaneously emerge in our calculations. The main contribution to the ground-state energy comes from short-range correlations in the wave function. Two-particle–two-hole excitations, included via CCSD, give the main contribution to the correlation energy [i.e., the energy in excess of the Hartree-Fock energy shown in Figs. 4(a) and 5(a)]. Here, the triples estimates are taken as 10% of the CCSD correlation energy, which was confirmed in benchmark calculations; see Appendix B. We see that the more spherical 0^+ ground state in ^{30}Ne resides about 1.8 MeV above the prolate 0^+ ground state. Binding energies are reproduced within about 3%, and angular-momentum projection would further reduce the small discrepancy. In contrast to ^{30}Ne, the energy difference between the competing spherical and prolate minima in ^{32}Mg is only a few tens of keV after angular-momentum projection. Thus, from our computations we cannot conclusively decide which state corresponds to the ground state in this nucleus. In addition, we do not study any level mixing

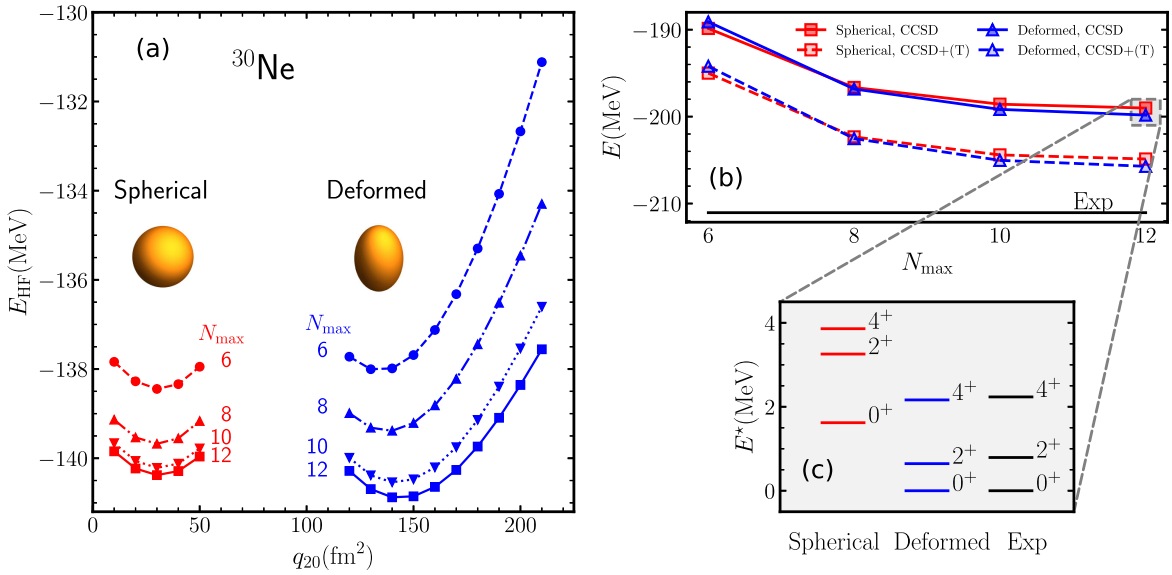

FIG. 4. (a) shows the Hartree-Fock energy for ^{30}Ne as a function of the quadrupole deformation q_{20} for the more spherical (left, red curves) and deformed (right, blue curves) states for increasingly larger model spaces (labeled by $N_{\max}$) with an oscillator frequency of $\hbar\omega = 14$ MeV. (b) demonstrates the convergence of the ground-state energy from symmetry-breaking coupled cluster with singles and doubles (CCSD) and triples estimates [CCSD + (T)]. These deformed states are superpositions of states with good angular momentum. (c) shows the rotational bands obtained from angular-momentum-projected coupled-cluster computations of the deformed states in a model space $N_{\max} = 8$. All calculations are based the interaction 1.8/2.0(EM).

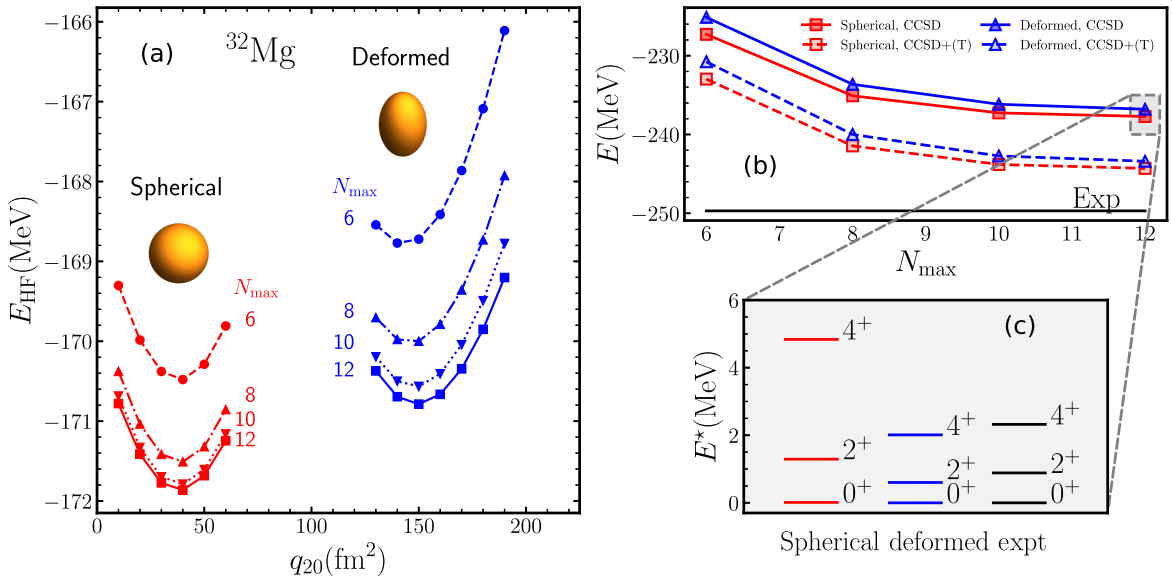

FIG. 5. The same as Fig. 4 but for ^{32}Mg.

and—at this moment—cannot compute the Hamiltonian matrix element between correlated states belonging to different deformations.

We also compute the energies for the near-spherical and the well-deformed minimum-energy configurations in ^{30}Ne and ^{32}Mg with the ΔNNLO$_{\rm GO}$(394) interaction and use a model space with $N_{\max} = 12$ and $\hbar\omega = 14$ MeV. We find unprojected CCSD ground-state energies of -195.9 and -196.0 MeV for the near-spherical and deformed configurations in ^{30}Ne, respectively, and -233.5 and -232.1 MeV for the corresponding states in ^{32}Mg. Thus, we also find shape coexistence with this interaction. We also see that the computed energies are close to those of the 1.8/2.0(EM) interaction that are

shown in Figs. 4(b) and 5(b). By adding the energy gain from projected Hartree-Fock, we find that the deformed configurations are the ground states in these nuclei.

C. Global sensitivity analysis of deformation

The *ab initio* computations presented in this work have a high resolution that allows one to study how individual terms corresponding to the 17 low-energy constants of a delta-full chiral interaction at NNLO [95], with regulator cutoff 394 MeV/c, impact nuclear deformation. To quantify this, we perform a variance-based global sensitivity analysis [61] of the $E(4^+)/E(2^+)$ ratio R_{42} in ^{20,32}Ne and ^{34}Mg. This dimensionless quantity signifies nuclear deformation [132] and emergent breaking of rotational symmetry [133]. It is sufficiently accurate to solve for the excited-state energies $E(2^+)$ and $E(4^+)$ in ^{20,32}Ne and ^{34}Mg using projection-after-variation Hartree-Fock, because the R_{42} values from Hartree-Fock and coupled-cluster theory are within 7% of each other (see Refs. [13,15] and Appendix B). However, the Monte Carlo sampling in a global sensitivity analysis requires prohibitively many projected Hartree-Fock computations. Indeed, we find it necessary to use one million samples to keep sampling uncertainties under control. To overcome this computational barrier, we develop fast and accurate emulators for the excitation energies using the method described in Sec. II F.

The strategy for training the emulator is similar to Ref. [64]. We generate 68 snapshots of the first excited 2^+ and 4^+ states, in the Hartree-Fock approximation, using values for the 17 low-energy constants according to a space-filling Latin hypercube design encompassing 20%–30% variation of their $\Delta\mathrm{NNLO}_{\mathrm{GO}}(394)$ values [95]. Figure 6 shows the accuracy of the resulting emulator for R_{42} as quantified by comparison with 400 exact projected Hartree-Fock calculations. The standard deviation of the differences indicates a relative precision of 1% (at the one-sigma level) for the interval of R_{42} values relevant to the global sensitivity analysis presented below. The excitation energies using our reduced-order model are accurate on the 10 keV level.

In the global sensitivity analysis, we numerically quantify, and decompose, the variances of the excitation energies for the ^{20,32}Ne and ^{34}Mg isotopes due to sampling one million different values of the low-energy constants at NNLO. The variances are decomposed in terms of the leading S-wave contacts $\tilde{C}_{^3S_1}$ and $\tilde{C}^{(\tau)}_{^1S_0}$ with $\tau = nn, np, pp$ denoting the isospin projections, the subleading contacts $C_{^1S_0}$, $C_{^3S_1}$, $C_{^3P_0}$, $C_{^1P_1}$, $C_{^3P_1}$, and $C_{^3P_2}$ (acting in a partial wave as indicated by the subscript), and C_{E_1} acting in the off-diagonal triplet $S-D$ channel. We also include the four subleading pion-nucleon couplings $c_{1,2,3,4}$, as well as the c_D and c_E couplings governing the strengths of the short-range three-nucleon potential. The variance integrals

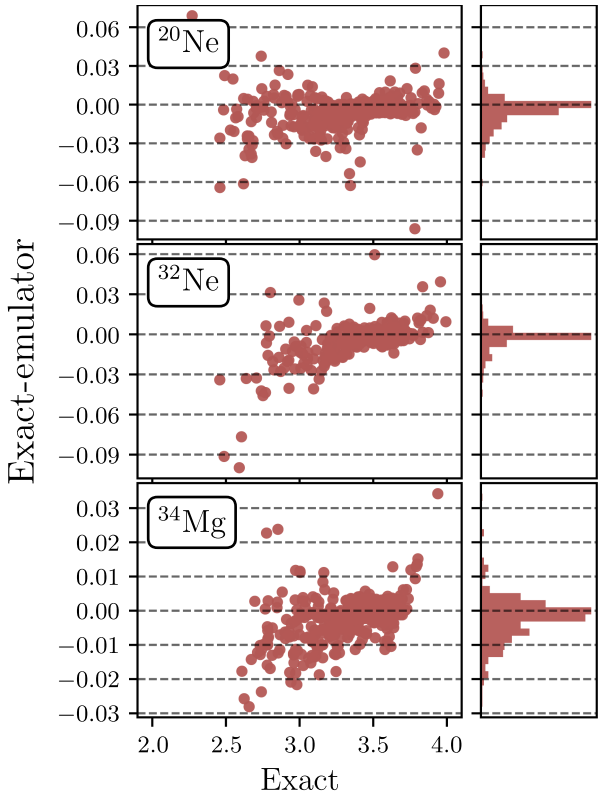

FIG. 6. Accuracy of R_{42} emulators as measured by the difference with respect to 400 exact Hartree-Fock calculations, on the y axis, as a function of R_{42} on the x axis. Shown are the subsets of results for which $R_{42} \in [2,4]$, i.e., the range relevant to the global sensitivity analysis. The horizontal dashed lines indicate precision, as they are spaced by two standard deviations of the projected histograms (shown in side panels).

underlying the sensitivity analysis are evaluated on a hypercubic domain centered on the $\Delta\mathrm{NNLO}_{\mathrm{GO}}(394)$ parametrization [95]. The size of the domain is based on recent Bayesian analyses [134,135] and naturalness arguments from effective field theory. In detail, we use ± 0.05 GeV^{-1} as the relevant range for each of the pion-nucleon couplings c_i and $\pm 0.05 \times 10^4$ GeV^{-4} for the subleading constants C_i. The leading-order contact couplings $\tilde{C}_i$ are somewhat small, and their intervals are limited to $\pm 0.005 \times 10^4$ GeV^{-2}. We examine our results for robustness by rescaling all side lengths of the hypercube by factors of $1/2$ and 2. Even larger domains result in noticeable higher-order sensitivities which we do not analyze further.

A majority of the samples in all three nuclei have $R_{42} \approx 10/3$ within 5%. This indicates that an axially deformed rigid rotor and emergent symmetry breaking is a robust feature of the effective field theory description of these nuclei. The variance of the conditional mean of R_{42}, with respect to a low-energy constant, divided by the total variance is a dimensionless ratio called the *main effect*. Overall, we find that more than 90% of the variance in R_{42}

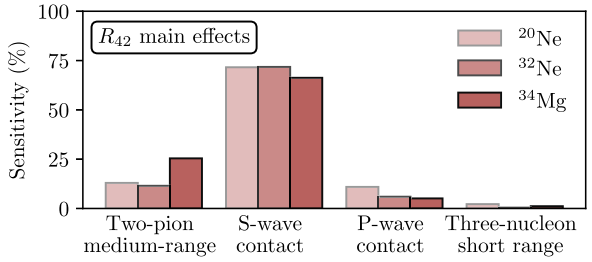

FIG. 7. Global sensitivity analysis of 10^6 emulations of projected Hartree-Fock computations in ^{20,32}Ne and ^{34}Mg using delta-full chiral effective field theory at next-to-next-to-leading order.

is explained via main effects. Figure 7 shows the main effects for R_{42} in ^{20,32}Ne and ^{34}Mg in terms of groups of low-energy constants proportional to medium-range two-pion exchange, short-range nucleon-nucleon contact interactions in the S and P waves, and the short-range three-nucleon interactions consisting of a contact interaction and pion exchange plus contact interaction. A greater value of the main effect indicates a larger sensitivity of R_{42} to the corresponding component of the chiral interaction. For all three nuclei, more than 50% of the deformation is driven by the S-wave contact part of the interaction. Adding short-range repulsion appears to increase deformation, probably by reducing pairing. Medium-range two-pion exchange is also important. Increasing its strength increases deformation, presumably by adding attraction in higher partial waves. The pion-nucleon couplings c_1, c_2, and c_3 enter prominently in the central potential of the two-pion exchange [136].

Figure 8 shows the main effects for R_{42} in ^{20,32}Ne and ^{34}Mg in more detail. For all three nuclei, about 40% of the deformation is driven by the subleading pion-nucleon coupling c_3 and the subleading singlet S-wave contact $C_{^1S_0}$. The c_3 coupling enters the attractive central part from the medium-range two-pion exchange in the nucleon-nucleon potential and also in the three-nucleon potential [136]. For ^{32}Ne and ^{34}Mg, with many more neutrons than ^{20}Ne, deformation becomes more sensitive to the isospin-breaking S-wave contact in the neutron-neutron channel. For ^{34}Mg, the ratio R_{42} appears to become more sensitive to the pion-nucleon coupling c_2. See Appendix E for the sensitivities of Hartree-Fock energies, including ground-state energies.

We can also use the posterior samples employed in Fig. 3 to probe what impacts deformation. The most relevant parts of the nuclear interaction can then be identified by studying correlations between the observable R_{42} in ^{32}Ne and individual low-energy constants. We find that the correlation is strongest for the S-wave contact term (with a correlation coefficient $r = 0.73$; i.e., an increase in the repulsive low-energy constant increases deformation), but it is also sizable for the three-nucleon contact interaction (see Appendix E for details). Comparing these results with the conditional variances from the global sensitivity analysis confirms the importance of pairing via the $^1S_0$ channel. We note that the domain of low-energy constants used in the global sensitivity analysis is smaller than the region spanned by the Bayesian posterior interaction ensemble.

Our sensitivity analysis is a first step, and the emerging picture is still incomplete. Indeed, we do not gauge the sensitivities of tensor and spin-orbit terms in the Hamiltonian that are independent of the low-energy constants. We also remind the reader that our potential lacks D-wave contacts beyond the off-diagonal triplet $S-D$ coupling, because these enter only at the next higher order. It will be interesting to compare more complete results with shell-model pictures about what drives nuclear deformation [37,38,48,137,138].

IV. SUMMARY AND DISCUSSION

In summary, we demonstrated how *ab initio* computations of nuclei can accurately describe binding energies, rotational bands, and collective electromagnetic transition strengths. These results were obtained in a nonperturbative framework where dynamical correlations were included via coupled-cluster theory and static correlations via angular-momentum projection. These advances allowed us to explore how collective nuclear properties are sensitive to specific terms in effective Hamiltonians of low-energy quantum chromodynamics that include nucleon-nucleon and three-nucleon forces. We found that the contacts in the

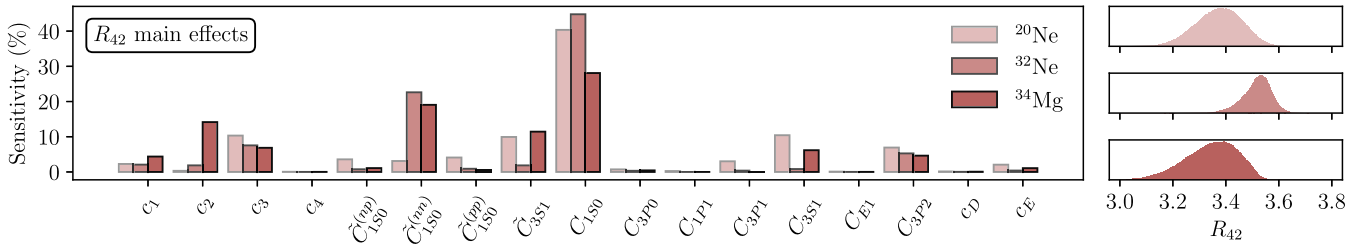

FIG. 8. Main effects for the R_{42} deformation measure in ^{20,32}Ne and ^{34}Mg from the low-energy constants as obtained in a global sensitivity analysis of 10^6 emulations of projected Hartree-Fock computations using delta-full chiral effective field theory at next-to-next-to-leading order. Distributions of R_{42} for ^{20}Ne, ^{32}Ne, and ^{34}Mg are also shown.

$^1S_0$ partial wave and the three-body contact play a major role in shaping nuclei. Using an ensemble of calibrated interactions, we made predictions with quantified uncertainties in neutron-rich neon nuclei. The uncertainties—while still considerable—are on par with experiment for the neon isotopes close to the neutron drip line. In particular, we predict shape coexistence in ^{30}Ne.

This work points to a conceptually simple and attractive multiscale picture of nuclei where the symmetry-breaking reference state contains the relevant physics aspects. Size-extensive methods then yield the lion's share of the binding energy, while symmetry-projection methods account for important collective components in the wave function that, however, contribute comparatively little to the binding energy.

Our computations demonstrate the predictive power of *ab initio* methods. This reductionist approach combines ever-increasing computational modeling capabilities and heuristic techniques to capture dynamical and emergent properties of complex systems. Other collective degrees of freedom (besides rotations) such as vibrations or competing shapes can be added in the same framework, because they can be realized as exponentiated one-body operators. Our sensitivity analysis provided first insights to the link between microscopic nuclear forces and complex nuclear phenomenology. The *ab initio* methods, and accompanying emulator techniques, developed in this work open for computational statistics analyses to identify principal components that drive emergent phenomena in finite systems. While we focused on an important problem in nuclear physics, similar challenges exist in quantum chemistry. Thus, we expect the novel symmetry-projection techniques of correlated states to be useful in many other applications.

ACKNOWLEDGMENTS

This work was supported (in part) by the U.S. Department of Energy, Office of Science, Office of Advanced Scientific Computing Research and Office of Nuclear Physics, Scientific Discovery through Advanced Computing (SciDAC) program (SciDAC-5 NUCLEI); by the U.S. Department of Energy, Office of Science, Office of Nuclear Physics, under Grants No. DE-FG02-96ER40963 and No. DE-SC0024465, and by the Quantum Science Center, a National Quantum Information Science Research Center of the U.S. Department of Energy; by the European Research Council (ERC) under the European Unions Horizon 2020 research and innovation program (Grant Agreement No. 758027); by the Swedish Research Council (Grants No. 2017-04234, No. 2020-05127, and No. 2021-04507). Computer time was provided by the Innovative and Novel Computational Impact on Theory and Experiment (INCITE) program. This research used resources of the Oak Ridge Leadership Computing Facility located at Oak Ridge National Laboratory, which is supported by the Office of Science of the Department of Energy under Contract No. DE-AC05-00OR22725, and resources provided by the Swedish National Infrastructure for Computing (SNIC) at Chalmers Centre for Computational Science and Engineering (C3SE) and the National Supercomputer Centre (NSC) partially funded by the Swedish Research Council through Grant Agreement No. 2018-05973. This manuscript has been authored by UT-Battelle, LLC under Contract No. DE-AC05-00OR22725 with the U.S. Department of Energy.

The U.S. Government retains and the publisher, by accepting the article for publication, acknowledges that the U.S. Government retains a nonexclusive, paid-up, irrevocable, worldwide license to publish or reproduce the published form of this manuscript, or allow others to do so, for U.S. Government purposes. The Department of Energy will provide public access to these results of federally sponsored research in accordance with the DOE public access plan [139].

APPENDIX A: OVERVIEW

The appendixes contain a number of details that support and further illuminate the results presented in the main text. Appendix B presents benchmarks and details about model-space dependencies for neon nuclei. We state our assumptions about various uncertainties in Appendix C. Appendix D presents details regarding results in magnesium isotopes. Finally, we give many more details about our global sensitivity analysis in Appendix E.

APPENDIX B: BENCHMARKS, MODEL-SPACE DEPENDENCE, AND GROUND-STATE ENERGIES FOR NEON ISOTOPES

For the computation of the ground-state energies of the $^{20-34}$Ne isotopes, we use the 1.8/2.0(EM) interaction and follow the approach in Ref. [107] and use a natural orbital basis and the coupled cluster with singles-doubles and leading-order triples excitations, known as the CCSDT-1 approximation [140,141]. The use of natural orbitals allows for converged CCSDT-1 calculations by imposing a cut on the product of occupation numbers for three particles above the Fermi surface and for three holes below the Fermi surface [107]. We use a model-space of 13 major oscillator shells with the oscillator frequency $\hbar\omega = 14$ MeV.

Figure 9 shows that binding energies are reproduced within about 3%. Angular-momentum projection is expected to further reduce the small discrepancy. We note that the triples correlation energy for all neon isotopes amounts to about 10% of the correlation energy from CCSD. This is consistent with findings for coupled-cluster computations of closed-shell spherical nuclei [20] and in quantum chemistry [33]. This justifies the triples estimates presented in Figs. 4 and 5 in the main text.

We turn to benchmarks with the symmetry-adapted no-core shell model (SA-NCSM) [9,11,16]. These are based

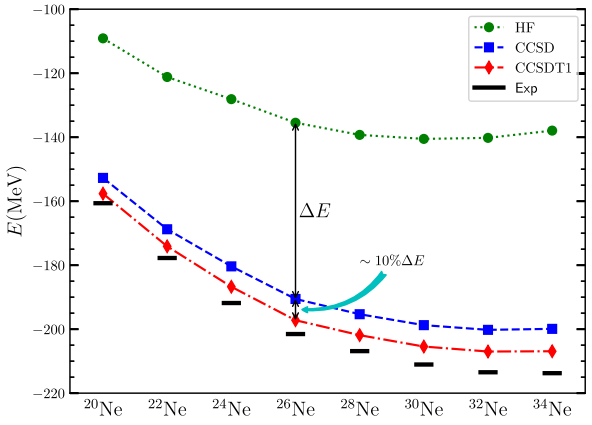

FIG. 9. Energies from the Hartree-Fock, CCSD, and CCSDT-1 approximations using the interaction 1.8/2.0(EM) from chiral effective field theory [31]. Results are based on a natural orbital basis built from 13 major oscillator shells with a frequency of $\hbar\omega = 14$ MeV. The triples correction amounts to about 10% of the correlation energy from CCSD (ΔE).

on the NNLO$_{\text{opt}}$ nucleon-nucleon interaction [112] and the ^{20}Ne nucleus. Figure 10 shows the 2^+ and 4^+ rotational states as a function of the oscillator frequency $\hbar\omega$ for model spaces consisting of $N_{\max}+1$ shells. We compare projection-after-variation results from Hartree-Fock with those from a "naive" (i.e., the left state is simply the adjoint of the reference state) and the bivariational coupled-cluster ansatz in Eq. (3), respectively. We see that both excited states are well converged with respect to the model-space size for Hartree-Fock. The coupled-cluster results exhibit a bit more model-space dependence. This might be because the disentangled coupled-cluster approach does not restore the broken symmetry exactly [15,34]. We also see that projected Hartree-Fock and the projected bivariational coupled-cluster are close to each other and to the SA-NCSM results. The "naive" coupled-cluster approach yields more compressed spectra. The agreement between Hartree-Fock and the much more expensive SA-NCSM and projected coupled-cluster results show how simple the physics behind rotational bands can be. This justifies the usage of a Hartree-Fock-based reduced-order model in the global sensitivity analysis of the ratio R_{42}. The accuracy of Hartree-Fock rotational bands is presumably limited to light nuclei, where superfluidity and pairing correlations are less important.

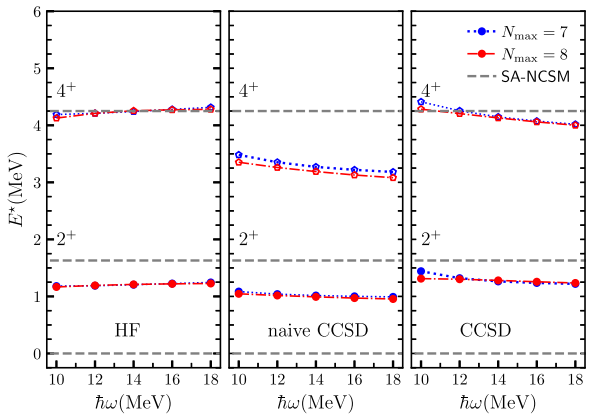

FIG. 10. Comparison between projection-after-variation Hartree-Fock (HF), naive projected coupled-cluster (naive CCSD), and projected coupled-cluster method (CCSD) for the excited 2^+ and 4^+ in ^{20}Ne using the NNLO$_{\text{opt}}$ nucleon-nucleon interaction. The dashed lines show benchmark results from the SA-NCSM [11].

We also compare R_{42} ratios from projected Hartree-Fock and coupled-cluster theory. Figure 10 shows that these are close in ^{20}Ne. For ^{32}Ne, using the 1.8/2.0(EM) interaction, we find $R_{42} = 3.49$ from Hartree-Fock and 3.25 from coupled-cluster theory. For ^{34}Ne, the corresponding values are $R_{42} = 3.46$ and 3.38, respectively.

We also want to benchmark the electric quadrupole transition strength. Our calculations are based on projected coupled-cluster theory, as described in Sec. II E. Figure 11 compares our computation of the $B(E2)$ strength in ^{20}Ne with the SA-NCSM results from Ref. [11], again for the nucleon-nucleon interaction NNLO$_{\text{opt}}$. Both results agree within uncertainties from finite model spaces. The benchmarks with the SA-NCSM give us confidence in the accuracy of our computations.

We turn to details regarding the results shown in Fig. 3 in the main text and focus on the interaction 1.8/2.0(EM). Figure 12 shows the energies of the 2^+ and 4^+ excited states in $^{20-34}$Ne and compares them to data for different model spaces (parametrized by the oscillator frequency $\hbar\omega$ and the number of shells $N_{\max+1}$). We find that the states are well converged with respect to model-space size. The variation of the results with respect to the model space is shown as an uncertainty in Fig. 3 in the main text. Our results for ^{20}Ne agree with those by Frosini *et al.* [14] using the same interaction.

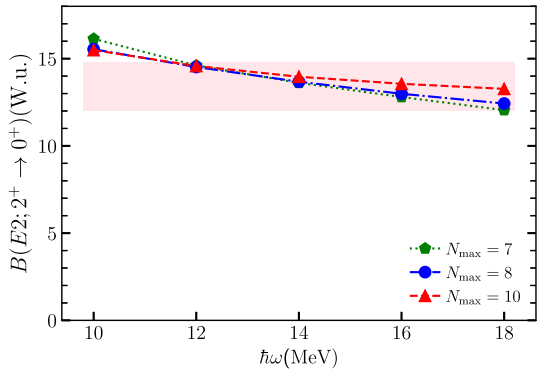

FIG. 11. Results from projected coupled-cluster method (CCSD) using the NNLO$_{\text{opt}}$ nucleon-nucleon interaction [112] for different model-space sizes ($N_{\max}$) and oscillator frequencies ($\hbar\omega$) and compared with the symmetry-adapted no-core shell model (red band) [11].

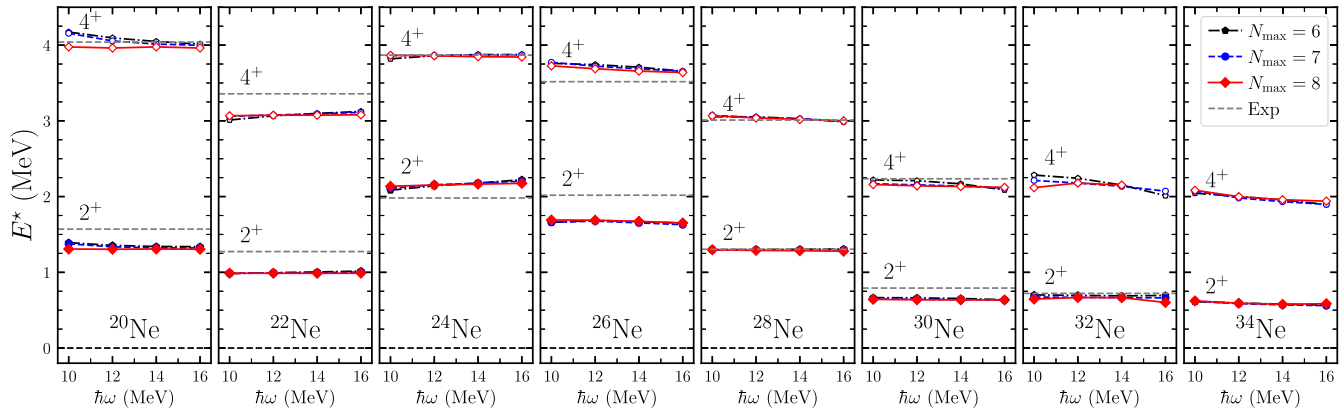

FIG. 12. Energies E of the lowest 2^+ and 4^+ states in even nuclei $^{20–34}$Ne, computed with the interaction 1.8/2.0(EM) from chiral effective field theory [31], shown as a function of the oscillator frequency and for various model spaces, and compared to data.

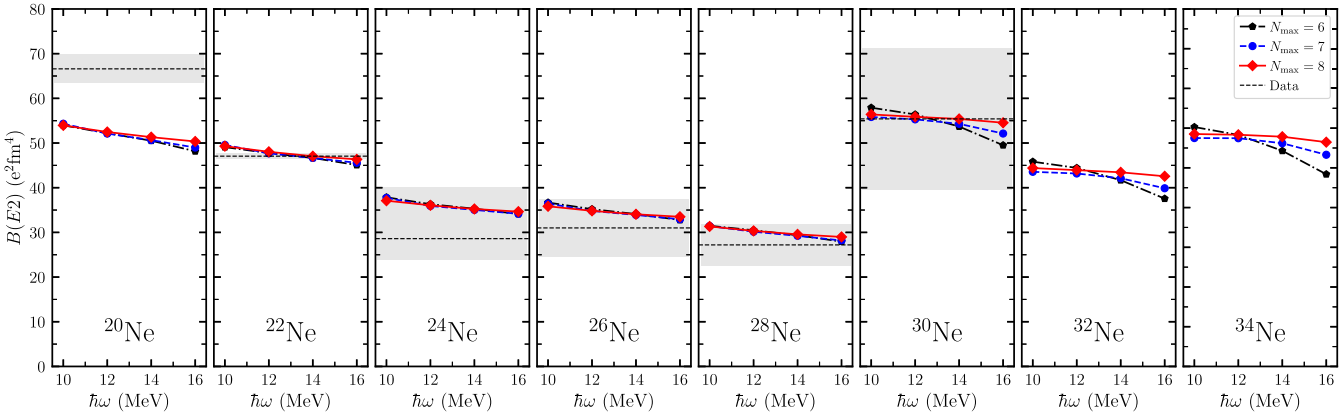

FIG. 13. $B(E2,\downarrow)$ computed with the interaction 1.8/2.0(EM) from chiral effective field theory [31] as a function of the oscillator frequency ($\hbar\omega$) for various model-space sizes ($N_{\max}$). Results are compared with available data (black dotted lines with gray uncertainty bands), taken from Ref. [131] for $^{20,24–28}$Ne, from Ref. [115] for ^{22}Ne, and from Ref. [130] for ^{30}Ne.

Figure 13 shows the $B(E2,\downarrow)$ for the transition between the first excited 2^+ state and the ground state in $^{20–34}$Ne obtained with the interaction 1.8/2.0(EM) and compared to available data for different model spaces (parametrized by the oscillator frequency $\hbar\omega$ and the number of shells $N_{\max+1}$). We find that the $B(E2,\downarrow)$ is well converged with respect to model-space size for isotopes with $N \geq 20$ while less so for neon nuclei with $N < 20$. The variation of the results with respect to the model space is shown as an uncertainty in the upper panel in Fig. 3 in the main text.

APPENDIX C: UNCERTAINTY ESTIMATES

The results based on the 1.8/2.0(EM) interaction include estimates of the method uncertainty coming from the use of method and model-space truncations. To estimate the latter, we considered the spread of results obtained for $N_{\max} = 6–8$ and $\hbar\omega = 10–16$ MeV (see Figs. 13 and 12). We assign (one-sigma) errors based on model-space truncations and on limitations of our method on our point predictions. This estimate is based on the spread of results from model-space truncations and from benchmarks with the no-core shell model. We find that model-space truncation errors are smaller than the estimated method truncation errors (see below).

For the delta-full NNLO interaction model, we employ the ensemble of Bayesian posterior samples and quantify both method and model uncertainties for predicted observables. We employ a fixed model space of $N_{\max} = 7$ and $\hbar\omega = 14$ MeV and assign normally distributed method errors with relative (one-sigma) errors of 10% (5%) for 2^+ (4^+) excitation energies (corresponding to about 100–150 keV). For the $B(E2,\downarrow)$, we assign a 15% (one-sigma) method error from our benchmark with the symmetry adapted no-core shell model [9] in ^{20}Ne; see Fig. 11. Moreover, we assign 10% (one-sigma) relative EFT truncation errors for all excitation energies and all transition strengths obtained with the ensemble of delta-full

NNLO interactions. We use experimental values to translate relative errors to absolute ones, and we use reference values of 1.0 and 2.5 MeV for 2^+ and 4^+ excitation energies, respectively (because these are the energy scales for the corresponding excitations), and 50 $e^2\mathrm{fm}^4$ for $B(E2,\downarrow)$ to get absolute errors for ^{32,34}Ne where experimental data are not available [because this is an estimate for $B(E2,\downarrow)$ in neon nuclei]. All errors are described by independent normal distributions.

APPENDIX D: DETAILS TO MAGNESIUM NUCLEI

Our studies of heavier magnesium nuclei are limited to using projection after variation of Hartree-Fock states. This simplification is justified based on Ref. [15] and the comparison of the rotational bands obtained from Hartree-Fock and coupled-cluster theory in the ^{20}Ne, as shown in Appendix B.

Figure 14 shows projected Hartree-Fock results for the energies $E(2^+)$ and $E(4^+)$ in $^{32-40}$Mg computed with the 1.8/2.0(EM) interaction as a function of the oscillator frequency $\hbar\omega$ in model spaces consisting of $N_{\max}+1$ shells. The results exhibit only a small model-space dependence and are close to data.

For ^{32}Mg, the Hartree-Fock results already confirm the shape coexistence in this nucleus [74]. While the spherical Hartree-Fock state is about 1 MeV lower in energy than the deformed one, the inclusion of short-range correlations via coupled-cluster theory reduces this difference.

Similarly, we see shape coexistence in ^{40}Mg, confirming the experimental [77] and theoretical results [41]. Our calculations of the drip line nucleus ^{40}Mg include couplings to the particle continuum via a Woods-Saxon basis consisting of bound and scattering states for the neutron $p_{3/2}$ partial wave, following Ref. [142].

One expects an inversion of the $p_{3/2}$ and $f_{7/2}$ single-particle orbitals close to the magnesium drip line. This is supported by the observation that ^{37}Mg is a deformed p-wave halo nucleus [143] and mean-field computations accounting for deformation and continuum coupling [144,145]. Indeed, our calculations for ^{38,40}Mg show an inversion of the $K^\pi = 7/2^-$ and $K^\pi = 1/2^-$ single-particle orbitals (where K denotes the single-particle angular-momentum component along the axial symmetry axis). We find that $^{34-40}$Mg are all prolate in their ground state, and the computed rotational bands are close to data.

Interestingly, for ^{40}Mg, we also find an oblate Hartree-Fock state that is close in energy to the prolate ground state. Performing coupled-cluster calculations for these two references, we find that the oblate band head is about 3 MeV above the prolate ground state, indicating an onset of shape coexistence and a possible interpretation of the third observed state [77]. This picture is also consistent with the Monte Carlo shell-model computations of Tsunoda *et al.* [41]. Figure 14 shows both the prolate and oblate 2^+ and 4^+ states, and we observe that the rotational structure of these two bands are very similar and close to that of a rigid rotor.

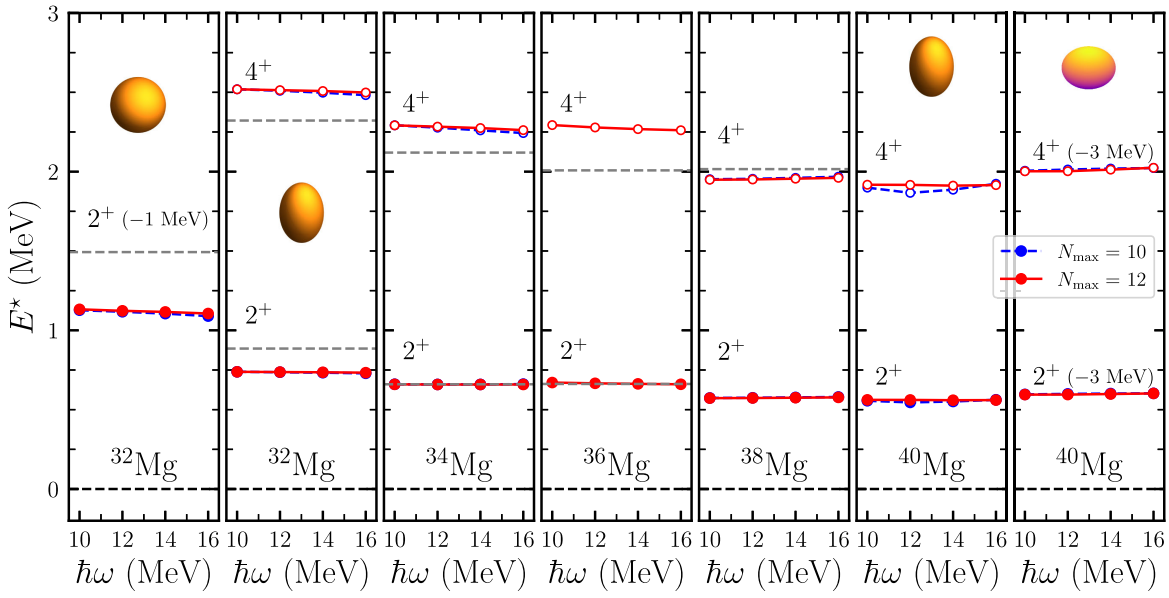

FIG. 14. Energies as a function of the oscillator frequency ($\hbar\omega$) and for various model spaces ($N_{\max}$), computed using projected Hartree-Fock with the chiral interaction 1.8/2.0(EM) [31] and compared to data (dashed horizontal lines). For ^{40}Mg, we show both the prolate and oblate rotational bands; the latter band head is about 3 MeV above the prolate ground state. The pictures show spherical, prolate deformed, and oblate deformed ellipsoids.

APPENDIX E: SENSITIVITY STUDY FOR NEON NUCLEI

Figure 15 shows the results from the sensitivity analysis of the energies $E(0^+)$, $E(2^+)$, and $E(4^+)$ in ^{20,32}Ne and ^{34}Mg. There are three main trends to observe. First, the variance of $E(0^+)$, i.e., the energy of the ground state, is explained to a great extent by the subleading pion-nucleon coupling c_2 and the leading S-wave contact $\tilde{C}_{^3S_1}$ in all three nuclei. The latter coupling is directly proportional to the deuteron binding energy. Second, the ground- and excited-state energies exhibit different main effect patterns, and this indicates that the structures of their respective wave functions likely differ. Third, for the energies, we also show the total effects [146] (white bars on top of colored bars of the main effects). They are nearly identical to the main effects, with some differences observed in ^{32}Ne, and this indicates that the (sum of) higher-order sensitivities are very small in the present domain.

Figure 16 shows the three strongest correlations between the low-energy constants of the delta-full NNLO Hamiltonian and the observables R_{42} and $E(2^+)$ of ^{32}Ne for the ensemble of Bayesian posterior interactions. We remind the reader that c_E is the low-energy constant of the three-body contact, while $\tilde{C}_{1S0np}$ and C_{1S0} are low-energy coefficients at (isospin-breaking) leading and next-to-leading order in the $^1S_0$ partial wave (the former acts in the neutron-proton channel of this partial wave).

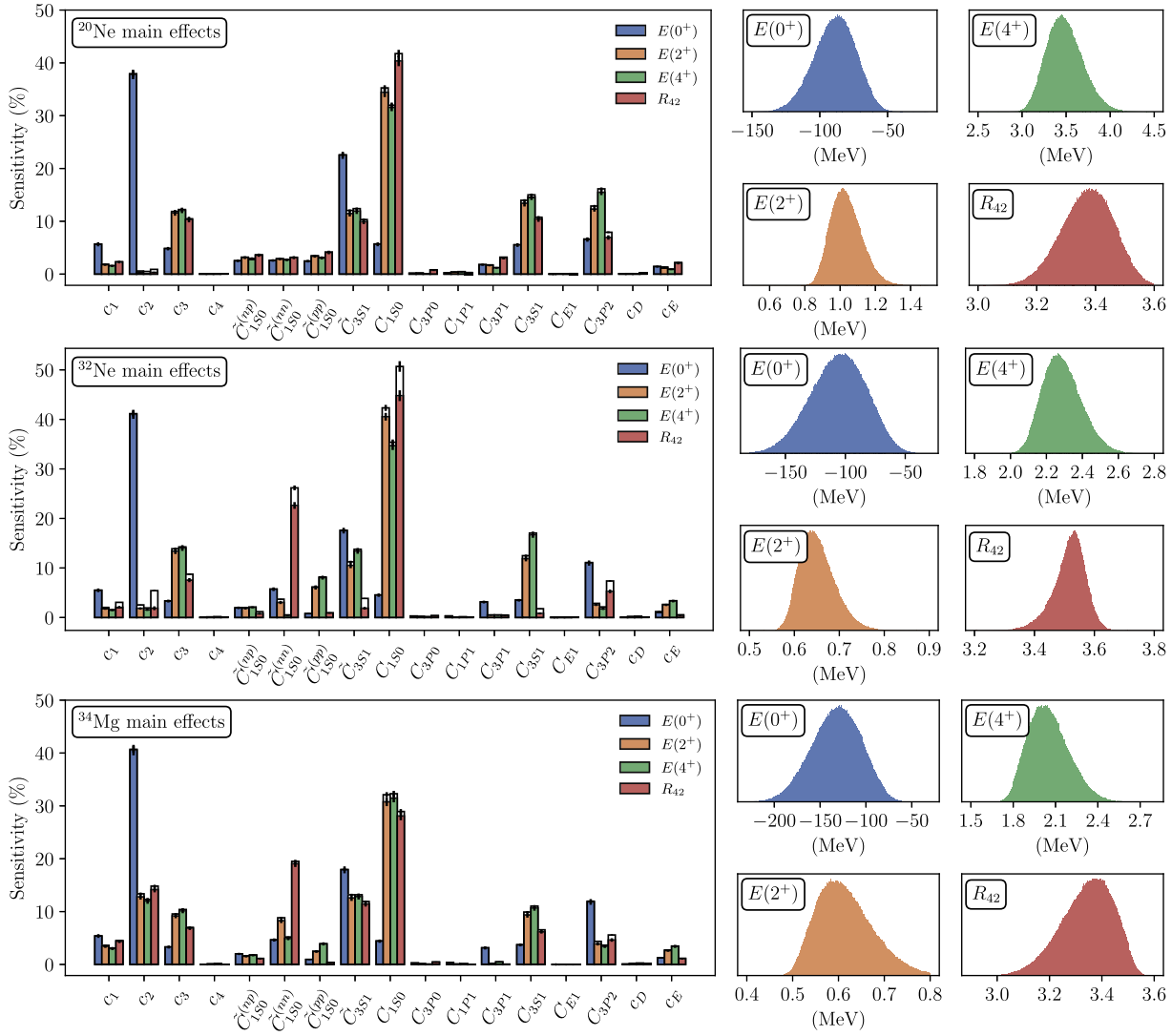

FIG. 15. Results of the global sensitivity analysis for the structure of ^{20,32}Ne and ^{34}Mg (top, center, and bottom). All Monte Carlo samples obtained as in the main text. Left: the main effects (colored bars) for R_{42} ground-state energy (E_{gs}) and excited 2^+ and 4^+ states. The vertical black bars indicate the respective 95% confidence intervals of the sensitivity indices as obtained using bootstrapped sampling. Here, we also include total effects (white bars on top). Groups of right four panels: histograms displaying the variation of the 1 179 648 samples for each output. All energies are obtained using an emulator based on eigenvector continuation of projected Hartree-Fock.

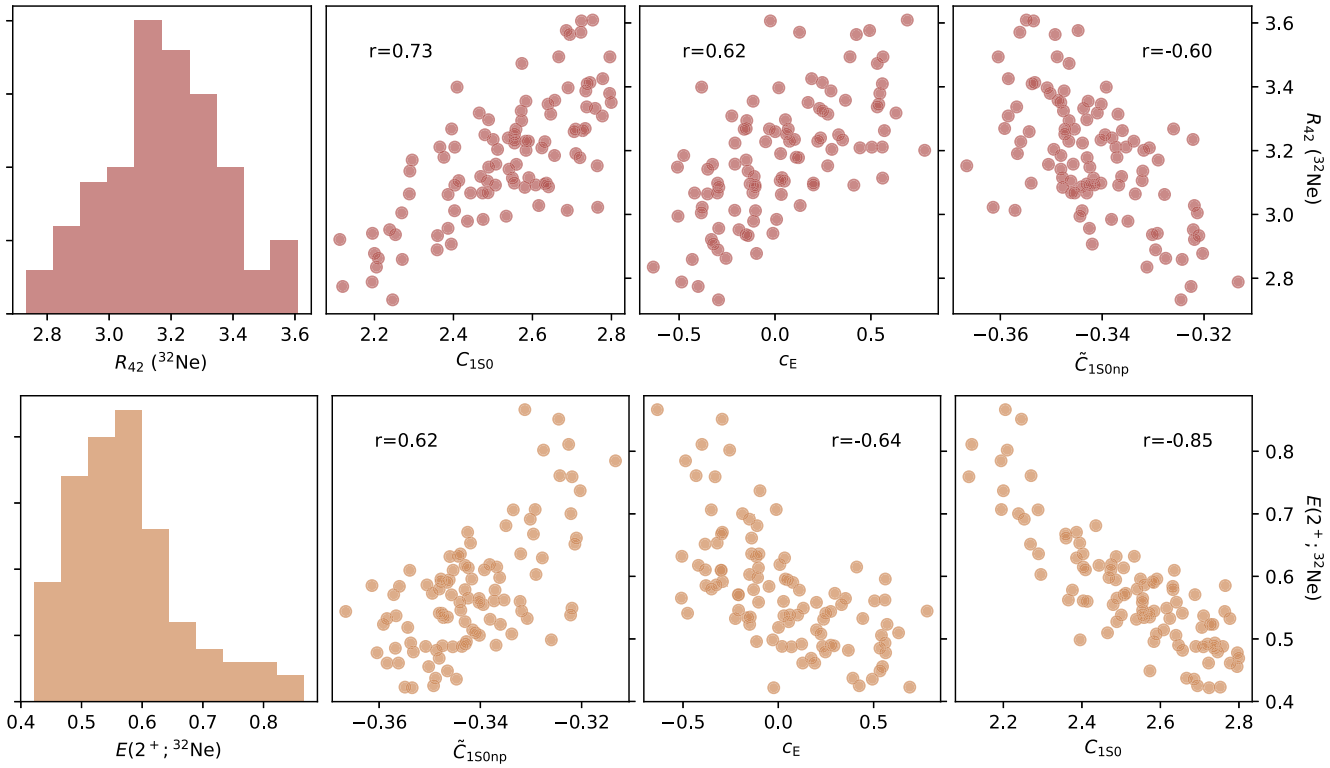

FIG. 16. Correlation between the low-energy constants of the delta-full next-to-next-to-leading-order Hamiltonian and the observables R_{42} (upper row) and $E(2+)$ (lower row) of ^{32}Ne. The scatter plots include the 100 interaction samples from the Bayesian posterior, while the histograms show the distribution for the respective observable. The Pearson correlation coefficient r is extracted for the samples for each pair of variables. All other low-energy constants have correlation coefficients with an absolute magnitude smaller than 0.4 and are not shown.

[1] A. Bohr and B. R. Mottelson, *Nuclear Structure* (W. A. Benjamin, Reading, MA, 1975), Vol. II: Nuclear Deformations.

[2] R. B. Wiringa, S. C. Pieper, J. Carlson, and V. R. Pandharipande, *Quantum Monte Carlo calculations of $a = 8$ nuclei*, Phys. Rev. C **62**, 014001 (2000).

[3] E. Epelbaum, H. Krebs, T. A. Lähde, D. Lee, and Ulf-G. Meißner, *Structure and rotations of the Hoyle state*, Phys. Rev. Lett. **109**, 252501 (2012).

[4] M. A. Caprio, P. Maris, J. P. Vary, and R. Smith, *Collective rotation from ab initio theory*, Int. J. Mod. Phys. E **24**, 1541002 (2015).

[5] P. Maris, M. A. Caprio, and J. P. Vary, *Emergence of rotational bands in ab initio no-core configuration interaction calculations of the Be isotopes*, Phys. Rev. C **91**, 014310 (2015).

[6] G. R. Jansen, M. D. Schuster, A. Signoracci, G. Hagen, and P. Navrátil, *Open sd-shell nuclei from first principles*, Phys. Rev. C **94**, 011301(R) (2016).

[7] T. Togashi, Y. Tsunoda, T. Otsuka, and N. Shimizu, *Quantum phase transition in the shape of Zr isotopes*, Phys. Rev. Lett. **117**, 172502 (2016).

[8] J. M. Yao, B. Bally, J. Engel, R. Wirth, T. R. Rodríguez, and H. Hergert, *Ab initio treatment of collective correlations and the neutrinoless double beta decay of ^{48}Ca*, Phys. Rev. Lett. **124**, 232501 (2020).

[9] T. Dytrych, K. D. Launey, J. P. Draayer, D. J. Rowe, J. L. Wood, G. Rosensteel, C. Bahri, D. Langr, and R. B. Baker, *Physics of nuclei: Key role of an emergent symmetry*, Phys. Rev. Lett. **124**, 042501 (2020).

[10] T. Miyagi, S. R. Stroberg, J. D. Holt, and N. Shimizu, *Ab initio multishell valence-space Hamiltonians and the island of inversion*, Phys. Rev. C **102**, 034320 (2020).

[11] K. D. Launey, T. Dytrych, G. H. Sargsyan, R. B. Baker, and J. P. Draayer, *Emergent symplectic symmetry in atomic nuclei*, Eur. Phys. J. Special Topics **229**, 2429 (2020).

[12] M. A. Caprio, P. J. Fasano, P. Maris, and A. E. McCoy, *Quadrupole moments and proton-neutron structure in p-shell mirror nuclei*, Phys. Rev. C **104**, 034319 (2021).

[13] M. Frosini, T. Duguet, J.-P. Ebran, B. Bally, T. Mongelli, T. R. Rodríguez, R. Roth, and V. Somà, *Multi-reference many-body perturbation theory for nuclei: II. Ab initio study of neon isotopes via PGCM and IM-NCSM calculations*, Eur. Phys. J. A **58**, 63 (2022).

[14] M. Frosini, T. Duguet, J. P. Ebran, B. Bally, H. Hergert, T. R. Rodríguez, R. Roth, J. M. Yao, and V. Somà, *Multi-reference many-body perturbation theory for nuclei*, Eur. Phys. J. A **58**, 64 (2022).

[15] G. Hagen, S. J. Novario, Z. H. Sun, T. Papenbrock, G. R. Jansen, J. G. Lietz, T. Duguet, and A. Tichai,

Angular-momentum projection in coupled-cluster theory: Structure of ^{34}Mg, Phys. Rev. C **105**, 064311 (2022).
[16] N. D. Heller, G. H. Sargsyan, K. D. Launey, C. W. Johnson, T. Dytrych, and J. P. Draayer, *New insights into backbending in the symmetry-adapted shell-model framework*, Phys. Rev. C **108**, 024304 (2023).
[17] F. Coester and H. Kümmel, *Short-range correlations in nuclear wave functions*, Nucl. Phys. **17**, 477 (1960).
[18] W. Dickhoff and C. Barbieri, *Self-consistent Green's function method for nuclei and nuclear matter*, Prog. Part. Nucl. Phys. **52**, 377 (2004).
[19] V. Somà, C. Barbieri, and T. Duguet, *Ab initio Gorkov-Green's function calculations of open-shell nuclei*, Phys. Rev. C **87**, 011303(R) (2013).
[20] G. Hagen, T. Papenbrock, M. Hjorth-Jensen, and D. J. Dean, *Coupled-cluster computations of atomic nuclei*, Rep. Prog. Phys. **77**, 096302 (2014).
[21] H. Hergert, S. K. Bogner, T. D. Morris, A. Schwenk, and K. Tsukiyama, *The in-medium similarity renormalization group: A novel ab initio method for nuclei*, Phys. Rep. **621**, 165 (2016).
[22] S. R. Stroberg, A. Calci, H. Hergert, J. D. Holt, S. K. Bogner, R. Roth, and A. Schwenk, *Nucleus-dependent valence-space approach to nuclear structure*, Phys. Rev. Lett. **118**, 032502 (2017).
[23] A. Ekström, C. Forssén, G. Hagen, G. R. Jansen, W. Jiang, and T. Papenbrock, *What is ab initio in nuclear theory?*, Front. Phys. **11**, 1129094 (2023).
[24] B. Hu, W. Jiang, T. Miyagi, Z. Sun, A. Ekström, C. Forssén, G. Hagen, J. D. Holt, T. Papenbrock, S. R. Stroberg, and I. Vernon, *Ab initio predictions link the neutron skin of* ^{208}Pb *to nuclear forces*, Nat. Phys. **18**, 1196 (2022).
[25] H. Iwasaki *et al.*, *Large collectivity of* ^{34}Mg, Phys. Lett. B **522**, 227 (2001).
[26] L. P. Gaffney *et al.*, *Studies of pear-shaped nuclei using accelerated radioactive beams*, Nature (London) **497**, 199 (2013).
[27] G. F. Bertsch, D. J. Dean, and W. Nazarewicz, *Computing atomic nuclei*, SciDAC Rev. **6**, 42 (2007), https://www.researchgate.net/publication/255220161_Computing_Atomic_Nuclei_The_Universal_Nuclear_Energy_Density_Functional.
[28] W. Nazarewicz, *Challenges in nuclear structure theory*, J. Phys. G **43**, 044002 (2016).
[29] S. K. Bogner, R. J. Furnstahl, and R. J. Perry, *Similarity renormalization group for nucleon-nucleon interactions*, Phys. Rev. C **75**, 061001(R) (2007).
[30] H. Kümmel, K. H. Lührmann, and J. G. Zabolitzky, *Many-fermion theory in expS- (or coupled cluster) form*, Phys. Rep. **36**, 1 (1978).
[31] K. Hebeler, S. K. Bogner, R. J. Furnstahl, A. Nogga, and A. Schwenk, *Improved nuclear matter calculations from chiral low-momentum interactions*, Phys. Rev. C **83**, 031301(R) (2011).
[32] Y. Kondo *et al.*, *First observation of* ^{28}O, Nature (London) **620**, 965 (2023).
[33] R. J. Bartlett and M. Musiał, *Coupled-cluster theory in quantum chemistry*, Rev. Mod. Phys. **79**, 291 (2007).
[34] Y. Qiu, T. M. Henderson, J. Zhao, and G. E. Scuseria, *Projected coupled cluster theory*, J. Chem. Phys. **147**, 064111 (2017).
[35] M. Baranger and K. Kumar, *Nuclear deformations in the pairing-plus-quadrupole model: (II). Discussion of validity of the model*, Nucl. Phys. **A110**, 490 (1968).
[36] K. Kumar and M. Baranger, *Nuclear deformations in the pairing-plus-quadrupole model: (III). Static nuclear shapes in the rare-earth region*, Nucl. Phys. **A110**, 529 (1968).
[37] P. Federman and S. Pittel, *Unified shell-model description of nuclear deformation*, Phys. Rev. C **20**, 820 (1979).
[38] W. Nazarewicz, *Microscopic origin of nuclear deformations*, Nucl. Phys. **A574**, 27 (1994).
[39] M. Dufour and A. P. Zuker, *Realistic collective nuclear Hamiltonian*, Phys. Rev. C **54**, 1641 (1996).
[40] A. Poves, *Shape coexistence and islands of inversion monopole vs multipole*, J. Phys. Soc. Jpn. Conf. Proc. **23**, 012015 (2018).
[41] N. Tsunoda, T. Otsuka, K. Takayanagi, N. Shimizu, T. Suzuki, Y. Utsuno, S. Yoshida, and H. Ueno, *The impact of nuclear shape on the emergence of the neutron dripline*, Nature (London) **587**, 66 (2020).
[42] A. Bohr, *The coupling of nuclear surface oscillations to the motion of individual nucleons*, Dan. Mat. Fys. Medd. **26**, 14 (1952), http://publ.royalacademy.dk/books/77/474?lang=da.
[43] A. Bohr and B. R. Mottelson, *Collective and individual-particle aspects of nuclear structure*, Dan. Mat. Fys. Medd. **27**, 16 (1953), http://publ.royalacademy.dk/books/76/460?lang=da.
[44] S. G. Nilsson, *Binding states of individual nucleons in strongly deformed nuclei*, K. Dan. Vidensk. Selsk. Mat. Fys. Medd. **29**, 16 (1955), http://publ.royalacademy.dk/books/75/441?lang=da.
[45] J. P. Elliott and J. D. Cockcroft, *Collective motion in the nuclear shell model. I. Classification schemes for states of mixed configurations*, Proc. R. Soc. A **245**, 128 (1958).
[46] J. P. N. Elliott and J. D. Cockcroft, *Collective motion in the nuclear shell model II. The introduction of intrinsic wave-functions*, Proc. R. Soc. A **245**, 562 (1958).
[47] A. P. Zuker and M. Dufour, *Separation of the monopole contribution to the nuclear Hamiltonian*, arXiv:nucl-th/9505012.
[48] J. Duflo and A. P. Zuker, *The nuclear monopole Hamiltonian*, Phys. Rev. C **59**, R2347 (1999).
[49] E. Caurier, G. Martínez-Pinedo, F. Nowack, A. Poves, and A. P. Zuker, *The shell model as a unified view of nuclear structure*, Rev. Mod. Phys. **77**, 427 (2005).
[50] J. Dobaczewski, W. Nazarewicz, J. Skalski, and T. Werner, *Nuclear deformation: A proton-neutron effect?*, Phys. Rev. Lett. **60**, 2254 (1988).
[51] T. R. Werner, J. Dobaczewski, M. W. Guidry, W. Nazarewicz, and J. Sheikh, *Microscopic aspects of nuclear deformation*, Nucl. Phys. **A578**, 1 (1994).
[52] M. V. Stoitsov, J. Dobaczewski, W. Nazarewicz, S. Pittel, and D. J. Dean, *Systematic study of deformed nuclei at the drip lines and beyond*, Phys. Rev. C **68**, 054312 (2003).
[53] J. P. Delaroche, M. Girod, J. Libert, H. Goutte, S. Hilaire, S. Péru, N. Pillet, and G. F. Bertsch, *Structure of even-even*

nuclei using a mapped collective Hamiltonian and the d1s Gogny interaction, Phys. Rev. C **81**, 014303 (2010).

[54] M. Kortelainen, J. McDonnell, W. Nazarewicz, P.-G. Reinhard, J. Sarich, N. Schunck, M. V. Stoitsov, and S. M. Wild, *Nuclear energy density optimization: Large deformations*, Phys. Rev. C **85**, 024304 (2012).

[55] S. E. Agbemava, A. V. Afanasjev, D. Ray, and P. Ring, *Global performance of covariant energy density functionals: Ground state observables of even-even nuclei and the estimate of theoretical uncertainties*, Phys. Rev. C **89**, 054320 (2014).

[56] T. Miyagi, S. R. Stroberg, J. D. Holt, and N. Shimizu, *Ab initio multishell valence-space Hamiltonians and the island of inversion*, Phys. Rev. C **102**, 034320 (2020).

[57] K. S. Becker, K. D. Launey, A. Ekström, and T. Dytrych, *Ab initio symmetry-adapted emulator for studying emergent collectivity and clustering in nuclei*, Front. Phys. **11**, 1064601 (2023).

[58] E. Epelbaum, H.-W. Hammer, and Ulf-G. Meißner, *Modern theory of nuclear forces*, Rev. Mod. Phys. **81**, 1773 (2009).

[59] R. Machleidt and D. Entem, *Chiral effective field theory and nuclear forces*, Phys. Rep. **503**, 1 (2011).

[60] H. W. Hammer, S. König, and U. van Kolck, *Nuclear effective field theory: Status and perspectives*, Rev. Mod. Phys. **92**, 025004 (2020).

[61] I. M. Sobol, *Global sensitivity indices for nonlinear mathematical models and their Monte Carlo estimates*, Math. Comput. Simul. **55**, 271 (2001).

[62] D. Frame, R. He, I. Ipsen, D. Lee, D. Lee, and E. Rrapaj, *Eigenvector continuation with subspace learning*, Phys. Rev. Lett. **121**, 032501 (2018).

[63] T. Duguet, A. Ekström, R. J. Furnstahl, S. König, and D. Lee, *Colloquium: Eigenvector continuation and projection-based emulators*, Rev. Mod. Phys. **96**, 031002 (2024).

[64] A. Ekström and G. Hagen, *Global sensitivity analysis of bulk properties of an atomic nucleus*, Phys. Rev. Lett. **123**, 252501 (2019).

[65] S. König, A. Ekström, K. Hebeler, D. Lee, and A. Schwenk, *Eigenvector continuation as an efficient and accurate emulator for uncertainty quantification*, Phys. Lett. B **810**, 135814 (2020).

[66] K. Heyde and J. L. Wood, *Shape coexistence in atomic nuclei*, Rev. Mod. Phys. **83**, 1467 (2011).

[67] A. Gade and S. N. Liddick, *Shape coexistence in neutron-rich nuclei*, J. Phys. G **43**, 024001 (2016).

[68] T. Otsuka, A. Gade, O. Sorlin, T. Suzuki, and Y. Utsuno, *Evolution of shell structure in exotic nuclei*, Rev. Mod. Phys. **92**, 015002 (2020).

[69] F. Nowacki, A. Obertelli, and A. Poves, *The neutron-rich edge of the nuclear landscape: Experiment and theory*, Prog. Part. Nucl. Phys. **120**, 103866 (2021).

[70] D. Bonatsos, A. Martinou, S. K. Peroulis, T. J. Mertzimekis, and N. Minkov, *Shape coexistence in even–even nuclei: A theoretical overview*, Atoms **11**, 117 (2023).

[71] T. Baumann, A. M. Amthor, D. Bazin, B. A. Brown, C. M. Folden, A. Gade, T. N. Ginter, M. Hausmann, M. Matos, D. J. Morrissey, M. Portillo, A. Schiller, B. M. Sherrill, A. Stolz, O. B. Tarasov, and M. Thoennessen, *Discovery of ^{40}Mg and ^{42}Al suggests neutron drip-line slant towards heavier isotopes*, Nature (London) **449**, 1022 (2007).

[72] W. Schwerdtfeger, P. G. Thirolf, K. Wimmer, D. Habs, H. Mach, T. R. Rodriguez, V. Bildstein, J. L. Egido, L. M. Fraile, R. Gernhäuser, R. Hertenberger, K. Heyde, P. Hoff, H. Hübel, U. Köster, T. Kröll, R. Krücken, R. Lutter, T. Morgan, and P. Ring, *Shape coexistence near neutron number $n = 20$: First identification of the $e0$ decay from the deformed first excited $J^\pi = 0^+$ state in ^{30}Mg*, Phys. Rev. Lett. **103**, 012501 (2009).

[73] P. Doornenbal *et al.*, *Spectroscopy of ^{32}Ne and the "island of inversion,"* Phys. Rev. Lett. **103**, 032501 (2009).

[74] K. Wimmer *et al.*, *Discovery of the shape coexisting 0^+ state in ^{32}Mg by a two neutron transfer reaction*, Phys. Rev. Lett. **105**, 252501 (2010).

[75] H. L. Crawford *et al.*, *Rotational band structure in ^{32}Mg*, Phys. Rev. C **93**, 031303(R) (2016).

[76] D. S. Ahn, N. Fukuda, H. Geissel, N. Inabe, N. Iwasa, T. Kubo, K. Kusaka, D. J. Morrissey, D. Murai, T. Nakamura, M. Ohtake, H. Otsu, H. Sato, B. M. Sherrill, Y. Shimizu, H. Suzuki, H. Takeda, O. B. Tarasov, H. Ueno, Y. Yanagisawa, and K. Yoshida, *Location of the neutron dripline at fluorine and neon*, Phys. Rev. Lett. **123**, 212501 (2019).

[77] H. L. Crawford *et al.*, *First spectroscopy of the near dripline nucleus ^{40}Mg*, Phys. Rev. Lett. **122**, 052501 (2019).

[78] M. Madurga *et al.*, *New isomeric transition in ^{36}Mg: Bridging the $n = 20$ and $n = 28$ islands of inversion*, Phys. Rev. C **109**, L061301 (2024).

[79] N. Kitamura *et al.*, *Coexisting normal and intruder configurations in 32Mg*, Phys. Lett. B **822**, 136682 (2021).

[80] A. O. Macchiavelli, H. L. Crawford, P. Fallon, R. M. Clark, and A. Poves, *Weak binding effects on the structure of ^{40}Mg*, Eur. Phys. J. A **58**, 66 (2022).

[81] P.-G. Reinhard, D. J. Dean, W. Nazarewicz, J. Dobaczewski, J. A. Maruhn, and M. R. Strayer, *Shape coexistence and the effective nucleon-nucleon interaction*, Phys. Rev. C **60**, 014316 (1999).

[82] R. Rodríguez-Guzmán, J. Egido, and L. Robledo, *Correlations beyond the mean field in magnesium isotopes: Angular momentum projection and configuration mixing*, Nucl. Phys. **A709**, 201 (2002).

[83] S. Péru and M. Martini, *Mean field based calculations with the Gogny force: Some theoretical tools to explore the nuclear structure*, Eur. Phys. J. A **50**, 88 (2014).

[84] E. Caurier, F. Nowacki, and A. Poves, *Merging of the islands of inversion at $n = 20$ and $n = 28$*, Phys. Rev. C **90**, 014302 (2014).

[85] I. Murray, M. MacCormick, D. Bazin, P. Doornenbal, N. Aoi, H. Baba, H. Crawford, P. Fallon, K. Li, J. Lee, M. Matsushita, T. Motobayashi, T. Otsuka, H. Sakurai, H. Scheit, D. Steppenbeck, S. Takeuchi, J. A. Tostevin, N. Tsunoda, Y. Utsuno, H. Wang, and K. Yoneda, *Spectroscopy of strongly deformed ^{32}Ne by proton knockout reactions*, Phys. Rev. C **99**, 011302(R) (2019).

[86] G. Hagen, T. Papenbrock, and D. J. Dean, *Solution of the center-of-mass problem in nuclear structure calculations*, Phys. Rev. Lett. **103**, 062503 (2009).

[87] G. Hagen, A. Ekström, C. Forssén, G. R. Jansen, W. Nazarewicz, T. Papenbrock, K. A. Wendt, S. Bacca, N.

Barnea, B. Carlsson, C. Drischler, K. Hebeler, M. Hjorth-Jensen, M. Miorelli, G. Orlandini, A. Schwenk, and J. Simonis, *Neutron and weak-charge distributions of the ^{48}Ca nucleus*, Nat. Phys. **12**, 186 (2016).

[88] G. Hagen, G. R. Jansen, and T. Papenbrock, *Structure of ^{78}Ni from first-principles computations*, Phys. Rev. Lett. **117**, 172501 (2016).

[89] J. Simonis, S. R. Stroberg, K. Hebeler, J. D. Holt, and A. Schwenk, *Saturation with chiral interactions and consequences for finite nuclei*, Phys. Rev. C **96**, 014303 (2017).

[90] T. D. Morris, J. Simonis, S. R. Stroberg, C. Stumpf, G. Hagen, J. D. Holt, G. R. Jansen, T. Papenbrock, R. Roth, and A. Schwenk, *Structure of the lightest tin isotopes*, Phys. Rev. Lett. **120**, 152503 (2018).

[91] P. Gysbers, G. Hagen, J. D. Holt, G. R. Jansen, T. D. Morris, P. Navrátil, T. Papenbrock, S. Quaglioni, A. Schwenk, S. R. Stroberg, and K. A. Wendt, *Discrepancy between experimental and theoretical β-decay rates resolved from first principles*, Nat. Phys. **15**, 428 (2019).

[92] K. Hebeler, V. Durant, J. Hoppe, M. Heinz, A. Schwenk, J. Simonis, and A. Tichai, *Normal ordering of three-nucleon interactions for ab initio calculations of heavy nuclei*, Phys. Rev. C **107**, 024310 (2023).

[93] D. R. Entem and R. Machleidt, *Accurate charge-dependent nucleon-nucleon potential at fourth order of chiral perturbation theory*, Phys. Rev. C **68**, 041001(R) (2003).

[94] A. Ekström, G. Hagen, T. D. Morris, T. Papenbrock, and P. D. Schwartz, *Δ isobars and nuclear saturation*, Phys. Rev. C **97**, 024332 (2018).

[95] W. G. Jiang, A. Ekström, C. Forssén, G. Hagen, G. R. Jansen, and T. Papenbrock, *Accurate bulk properties of nuclei from $a = 2$ to ∞ from potentials with Δ isobars*, Phys. Rev. C **102**, 054301 (2020).

[96] I. Vernon, M. Goldstein, and R. G. Bower, *Galaxy formation: A Bayesian uncertainty analysis*, Bayesian Anal. **5**, 619 (2010).

[97] I. Vernon, J. Liu, M. Goldstein, J. Rowe, J. Topping, and K. Lindsey, *Bayesian uncertainty analysis for complex systems biology models: Emulation, global parameter searches and evaluation of gene functions*, BMC Syst. Biol. **12**, 1 (2018).

[98] A. F. M. Smith and A. E. Gelfand, *Bayesian statistics without tears: A sampling-resampling perspective*, Am. Stat. **46**, 84 (1992).

[99] W. Jiang and C. Forssén, *Bayesian probability updates using sampling/importance resampling: Applications in nuclear theory*, Front. Phys. **10**, 1058809 (2022).

[100] D. Siemens, J. R. de Elvira, E. Epelbaum, M. Hoferichter, H. Krebs, B. Kubis, and U.-G. Meißner, *Reconciling threshold and subthreshold expansions for pion-nucleon scattering*, Phys. Lett. B **770**, 27 (2017).

[101] G. Hagen, T. Papenbrock, D. J. Dean, A. Schwenk, A. Nogga, M. Włoch, and P. Piecuch, *Coupled-cluster theory for three-body Hamiltonians*, Phys. Rev. C **76**, 034302 (2007).

[102] R. Roth, S. Binder, K. Vobig, A. Calci, J. Langhammer, and P. Navrátil, *Medium-mass nuclei with normal-ordered chiral NN+3N interactions*, Phys. Rev. Lett. **109**, 052501 (2012).

[103] S. Binder, P. Piecuch, A. Calci, J. Langhammer, P. Navrátil, and R. Roth, *Extension of coupled-cluster theory with a noniterative treatment of connected triply excited clusters to three-body Hamiltonians*, Phys. Rev. C **88**, 054319 (2013).

[104] M. Frosini, T. Duguet, B. Bally, Y. Beaujeault-Taudière, J. P. Ebran, and V. Somà, *In-medium k-body reduction of n-body operators: A flexible symmetry-conserving approach based on the sole one-body density matrix*, Eur. Phys. J. A **57**, 151 (2021).

[105] A. Staszczak, M. Stoitsov, A. Baran, and W. Nazarewicz, *Augmented Lagrangian method for constrained nuclear density functional theory*, Eur. Phys. J. A **46**, 85 (2010).

[106] R. F. Bishop, *An overview of coupled cluster theory and its applications in physics*, Theor. Chim. Acta **80**, 95 (1991).

[107] S. J. Novario, G. Hagen, G. R. Jansen, and T. Papenbrock, *Charge radii of exotic neon and magnesium isotopes*, Phys. Rev. C **102**, 051303(R) (2020).

[108] J. Arponen, *The method of stationary cluster amplitudes and the phase transition in the Lipkin pseudospin model*, J. Phys. G **8**, L129 (1982).

[109] J. Arponen, *Variational principles and linked-cluster exp S expansions for static and dynamic many-body problems*, Ann. Phys. (N.Y.) **151**, 311 (1983).

[110] G. Hagen, T. Papenbrock, D. J. Dean, M. Hjorth-Jensen, and B. Velamur Asokan, *Ab initio computation of neutron-rich oxygen isotopes*, Phys. Rev. C **80**, 021306(R) (2009).

[111] D. J. Thouless, *Stability conditions and nuclear rotations in the Hartree-Fock theory*, Nucl. Phys. **21**, 225 (1960).

[112] A. Ekström, G. Baardsen, C. Forssén, G. Hagen, M. Hjorth-Jensen, G. R. Jansen, R. Machleidt, W. Nazarewicz, T. Papenbrock, J. Sarich, and S. M. Wild, *Optimized chiral nucleon-nucleon interaction at next-to-next-to-leading order*, Phys. Rev. Lett. **110**, 192502 (2013).

[113] B. Bally and T. Duguet, *Norm overlap between many-body states: Uncorrelated overlap between arbitrary Bogoliubov product states*, Phys. Rev. C **97**, 024304 (2018).

[114] N. M. Parzuchowski, S. R. Stroberg, P. Navrátil, H. Hergert, and S. K. Bogner, *Ab initio electromagnetic observables with the in-medium similarity renormalization group*, Phys. Rev. C **96**, 034324 (2017).

[115] J. Henderson *et al.*, *Testing microscopically derived descriptions of nuclear collectivity: Coulomb excitation of ^{22}Mg*, Phys. Lett. B **782**, 468 (2018).

[116] S. R. Stroberg, J. Henderson, G. Hackman, P. Ruotsalainen, G. Hagen, and J. D. Holt, *Systematics of E2 strength in the sd shell with the valence-space in-medium similarity renormalization group*, Phys. Rev. C **105**, 034333 (2022).

[117] B. Bally and M. Bender, *Projection on particle number and angular momentum: Example of triaxial Bogoliubov quasiparticle states*, Phys. Rev. C **103**, 024315 (2021).

[118] J. Fujita and H. Miyazawa, *Pion theory of three-body forces*, Prog. Theor. Phys. **17**, 360 (1957).

[119] D. L. Hill and J. A. Wheeler, *Nuclear constitution and the interpretation of fission phenomena*, Phys. Rev. **89**, 1102 (1953).

[120] J. J. Griffin and J. A. Wheeler, *Collective motions in nuclei by the method of generator coordinates*, Phys. Rev. **108**, 311 (1957).

[121] P.-O. Löwdin, *Quantum theory of many-particle systems. II. Study of the ordinary Hartree-Fock approximation*, Phys. Rev. **97**, 1490 (1955).

[122] C. A. Jiménez-Hoyos, T. M. Henderson, T. Tsuchimochi, and G. E. Scuseria, *Projected Hartree-Fock theory*, J. Chem. Phys. **136**, 164109 (2012).

[123] J. Rodriguez-Laguna, L. M. Robledo, and J. Dukelsky, *Efficient computation of matrix elements of generic slater determinants*, Phys. Rev. A **101**, 012105 (2020).

[124] H. G. A. Burton, *Generalized nonorthogonal matrix elements: Unifying Wick's theorem and the Slater-Condon rules*, J. Chem. Phys. **154**, 144109 (2021).

[125] H. Hergert, *A guided tour of ab initio nuclear many-body theory*, Front. Phys. **8**, 00379 (2020).

[126] Evaluated nuclear structure data file (ENSDF), https://www.nndc.bnl.gov/ensdfarchivals/.

[127] B. A. Brown and W. A. Richter, *New "usd" Hamiltonians for the sd shell*, Phys. Rev. C **74**, 034315 (2006).

[128] M. G. Mayer and J. H. D. Jensen, *Elementary Theory of Nuclear Shell Structure* (John Wiley & Sons, New York, 1955).

[129] Y. Yanagisawa *et al.*, *The first excited state of* ^{30}Ne *studied by proton inelastic scattering in reversed kinematics*, Phys. Lett. B **566**, 84 (2003).

[130] P. Doornenbal, H. Scheit, S. Takeuchi, N. Aoi, K. Li, M. Matsushita, D. Steppenbeck, H. Wang, H. Baba, E. Ideguchi, N. Kobayashi, Y. Kondo, J. Lee, S. Michimasa, T. Motobayashi, A. Poves, H. Sakurai, M. Takechi, Y. Togano, and K. Yoneda, *Mapping the deformation in the "island of inversion": Inelastic scattering of* ^{30}Ne *and* ^{36}Mg *at intermediate energies*, Phys. Rev. C **93**, 044306 (2016).

[131] B. Pritychenko, M. Birch, B. Singh, and M. Horoi, *Tables of $E2$ transition probabilities from the first 2^+ states in even-even nuclei*, At. Data Nucl. Data Tables **107**, 1 (2016).

[132] R. F. Casten, *Nuclear Structure from a Simple Perspective*, Oxford Studies in Nuclear Physics Vol. 13 (Oxford University Press, New York, 1990).

[133] T. Papenbrock, *Effective theory for deformed nuclei*, Nucl. Phys. **A852**, 36 (2011).

[134] S. Wesolowski, I. Svensson, A. Ekström, C. Forssén, R. J. Furnstahl, J. A. Melendez, and D. R. Phillips, *Rigorous constraints on three-nucleon forces in chiral effective field theory from fast and accurate calculations of few-body observables*, Phys. Rev. C **104**, 064001 (2021).

[135] I. Svensson, A. Ekström, and C. Forssén, *Inference of the low-energy constants in Δ-full chiral effective field theory including a correlated truncation error*, Phys. Rev. C **109**, 064003 (2024).

[136] H. Krebs, E. Epelbaum, and U. G. Meißner, *Nuclear forces with Δ excitations up to next-to-next-to-leading order, part I: Peripheral nucleon-nucleon waves*, Eur. Phys. J. A **32**, 127 (2007).

[137] T. Otsuka, T. Matsuo, and D. Abe, *Mean field with tensor force and shell structure of exotic nuclei*, Phys. Rev. Lett. **97**, 162501 (2006).

[138] A. Poves, *Shape coexistence: The shell model view*, J. Phys. G **43**, 024010 (2016).

[139] http://energy.gov/downloads/doe-public-access-plan.

[140] Y. S. Lee, S. A. Kucharski, and R. J. Bartlett, *A coupled cluster approach with triple excitations*, J. Chem. Phys. **81**, 5906 (1984).

[141] J. D. Watts and R. J. Bartlett, *Economical triple excitation equation-of-motion coupled-cluster methods for excitation energies*, Chem. Phys. Lett. **233**, 81 (1995).

[142] G. Hagen, M. Hjorth-Jensen, G. R. Jansen, and T. Papenbrock, *Emergent properties of nuclei from ab initio coupled-cluster calculations*, Phys. Scr. **91**, 063006 (2016).

[143] N. Kobayashi *et al.*, *Observation of a p-wave one-neutron halo configuration in* ^{37}Mg, Phys. Rev. Lett. **112**, 242501 (2014).

[144] I. Hamamoto, *Neutron shell structure and deformation in neutron-drip-line nuclei*, Phys. Rev. C **85**, 064329 (2012).

[145] I. Hamamoto, *Shell structure of one-particle resonances in deformed potentials*, Phys. Rev. C **93**, 054328 (2016).

[146] A. Saltelli, P. Annoni, I. Azzini, F. Campolongo, M. Ratto, and S. Tarantola, *Variance based sensitivity analysis of model output. Design and estimator for the total sensitivity index*, Comput. Phys. Commun. **181**, 259 (2010).